Linear Array Photodiode and Data Acquisition System Development for Multi-Point Line FLDI Measurements

Joshua M. Weisberger*, Brett F. Bathel†, Joseph W. Lee‡
NASA Langley Research Center, Hampton, VA, 23681

Angelo A. Cavone§
Analytical Mechanics Associates, Hampton, VA, 23681

The continuous development and advancement of multi-point line focused laser differential interferometry (FLDI) instruments requires larger numbers of acquisition channels to make more finely spatially resolved measurements of high-frequency flow fluctuations. No current off-the-shelf system exists for these line FLDI measurements, and so a single unified system consisting of a linear array photodiode, required electronics, and a data acquisition system has been developed to enhance the measurement resolution, both spatially and temporally. A printed circuit board was developed on which the linear array photodiode is mounted for inclusion into an existing FLDI system, and amplifier breakout boards incorporate electronics to condition the signal for the data acquisition system while retaining the necessary high frequency response. The data acquisition system uses a National Instruments® chassis and multiple oscilloscope modules, with a specially-designed LabVIEW® user interface for laboratory and wind tunnel setup, calibration, and testing. Details regarding the development of the linear array photodiode system and the data acquisition system are provided, and systematic testing of all components is presented, culminating in a test of the system integrated into an existing line FLDI system for measurements of a turbulent jet.

I. Introduction

Focused laser differential interferometry (FLDI) has become a staple measurement technique for non-intrusive, weak, high frequency fluctuation measurements in both the laboratory setting and particularly in wind tunnels, where hot-wire anemometers and other physical, intrusive probes have typically dominated. Recent developments of FLDI systems have tended toward larger numbers of acquisition channels (two or more). With the introduction of a line FLDI system ([1, 2]), the need for higher quality electronic circuitry and data acquisition systems has become important.

There are several single-element photodiodes that have been used consistently for FLDI measurements by different research groups, including the Thorlabs® FDS100 [3–7], DET36A(2) [8–15], PDA36A2 [16–24], DET100A2 [25, 26], PDA10A2 [19], PDB210A (large-area balanced amplified photodetector) [27], and the Ultrafast Sensors™ SDX318 (balanced photoreceiver) [27, 28]. Separate amplifier systems are sometimes used to increase the output voltage signal, including the Stanford Research Systems™ SR445 and SR560 units. Two groups currently developing line/multi-point FLDI systems utilize different approaches. The first used a Hamamatsu® S8558 16-channel linear array photodiode [1, 2]. The second uses fibers to couple each individual beam into separate single-element photodiodes [20, 21].

Variation in the data acquisition systems used between research groups is also common. Systems that have been used include the Cleverscope™ CS328A-XSE [3–7, 12] and CS320A [10], the Pico Technology PicoScope® model 5443B [29], model 5442D [9, 13], model 5444D [11, 15], and model 2204A [8], the Keysight InfiniiVision® DSOX4024A [30], the Yokogawa® DL850 [16, 17], and the Tektronix® 6 Series MSO [25, 31]. National Instruments® (NI) chassis/module combinations have also been used. The current authors used an NI PXIe-1062Q chassis with two PXIe-5171r 8-channel scope modules for the measurements in Refs. [1, 2], while others use the NI PXIe-8381, BNC-2110, and PXIe-6368 combination [20, 22, 24], or a USB-6356 [18].

*Research Engineer, Advanced Measurements and Data Systems Branch, AIAA Member.
†Research Engineer, Advanced Measurements and Data Systems Branch, AIAA Senior Member.
‡Electronics Technician, Advanced Measurements and Data Systems Branch.
§Research Engineer, Advanced Measurements and Data Systems Branch.

There is no single best acquisition system for FLDI measurements, and the researcher must weigh the benefits and limitations of each photodiode/data acquisition system combination for each application. The system described in this paper outlines the development of a specifically tailored line FLDI data acquisition system for a 35-channel linear array photodiode. In Section II, an overview of the line FLDI system is presented to motivate the need for the development of this photodiode/data acquisition system. In Section III, the design, implementation, and testing of the amplifier circuitry required for the selected linear array photodiode is discussed. In Section IV, the coupling of this amplifier system to the data acquisition system is discussed, including the reasoning behind, and explanation of, the LabVIEW® graphical user interface development since its previous use in Refs. [1, 2]. Section V then systematically tests each aspect of the line FLDI systems, and culminates in a simple demonstration of the system in use to measure the flow fluctuations of a compressed air jet issuing from a small diameter nozzle. The goal of this paper is to provide details of the development of this measurement technique that are typically not included in the literature, in the hopes that it may provide a more concrete starting point for others that wish to develop a higher channel-count measurement capability that can be used for, but is not limited to, multi-point line FLDI systems.

II. Line FLDI Setup and Alignment

A schematic of the line FLDI system is shown in Fig. 1. The system used for testing in this study is only a single-line version, and the description of the two-line FLDI system can be found in Refs. [1, 2]. Laser L directs a 0.7 mm diameter beam of 532 nm light toward mirrors M^{1P} and M^{2P}, which reflect the light onto the main optical axis, and allow for simple beam centering alignments. The beam passes through a half-wave plate (HWP^{1P}) prior to entering the polarizing beamsplitter cube (PBS), allowing for variable attenuation of the beam intensity transmitted through the system; the PBS reflects the unwanted linearly horizontally polarized (LHP) light into the beam dump BD, while allowing linearly vertically polarized (LVP) light to transmit through. A second half-wave plate (HWP^{2P}) rotates the linearly polarized light by twice the angle between the LVP light and the fast axis of HWP^{2P}, maintaining the linearity of the polarization state. The beam, still collimated, then passes through a beam expander optic, BE (a short focal length lens). As the beam expands, it passes through a positive cylindrical lens (PCL^{P}), placed such that it is one focal length away from the focus of BE, and thus collimating the beam in the y-direction (see color key at the top of Fig. 1). The beam now continues to expand in the x-direction and remains collimated in the y-direction as it passes through a Wollaston prism (W^{P}), which splits the beam into two beams in the x-direction, separated by an angle α and orthogonally linearly polarized to one another. Equal splitting of the beam intensity into these two separate beams occurs when the linear polarization of the input beam to W^{P} is oriented such that it is angled 45° from the axis of splitting (or halfway between the x and y axes in this schematic). Note that HWP^{2P} can also be replaced with an appropriately oriented quarter-wave plate, which allows for simpler realignment of the system when the FLDI line is rotated. These two separate beams continue to diverge in the x-direction while remaining collimated in the y-direction. A negative cylindrical lens (NCL^{P}) is oriented such that the collimated beam in the y-direction begins to diverge slightly, and is positioned such that its focal point lies at the

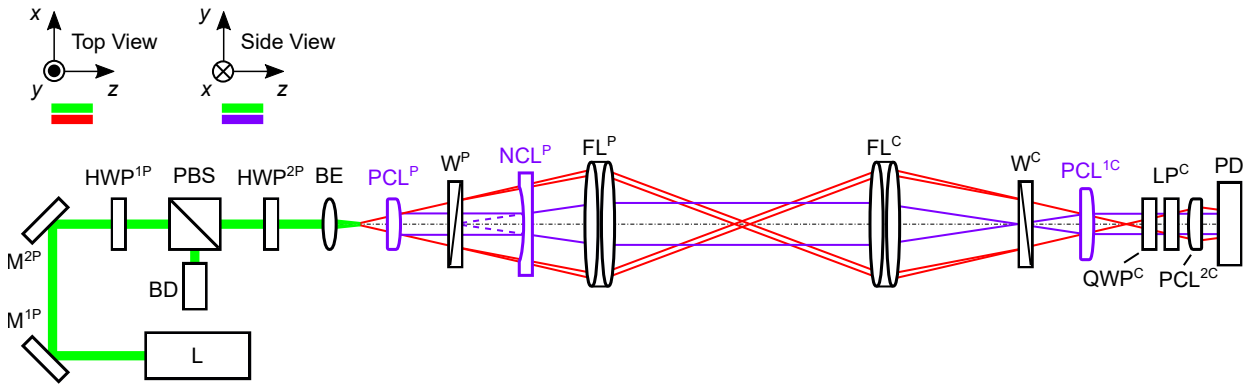

Fig. 1 Schematic of a single-line FLDI system, with *pitch* side on the left and *catch* side on the right. Colors of the light rays and some optics correspond to different axis orientations as defined in the color key above the schematic.

center of W^P. This lens does not alter the light diverging in the x-direction. When the beam reaches the field lens (FL^P), the positioning of both BE and NCL^P results in a beam that is again collimated in the y-direction, but focuses down (i.e., converges) in the x-direction.

On the catch side of the system, the position of FL^C and W^C mirrors that of the pitch side exactly. FL^C focuses the beam down in both x- and y-directions, with the y-direction focusing down at the center of W^C, and then continuing to expand after. At W^C, the two x-direction beams are made coincident again, and continue to focus down after. Another positive cylindrical lens (PCL^{1C}) is positioned and oriented such that it allows the x-direction beam to continue to focus down, while collimating the beam in the y-direction. The beam passes through a quarter-wave plate (QWP^C) which is used to null out any ellipticity in the beam polarization, and then through a linear polarizer (LP^C) which is used as a polarization analyzer to make the orthogonal polarization states interfere with each other. A final positive cylindrical lens (PCL^{2C}) is oriented such that it only affects the x-direction beam, and is used to loosely focus the converging beam onto the photodiode linear array (PD).

Fig. 2 Effect of adjustment of the focal length or position of (a) PCL^{1C} or (b) PCL^{2C} on the beam size incident on PD (compare colored solid outline and colored filled shape).

Adjustment of the laser line on PD can be accomplished by moving PCL^{1C} and PCL^{2C}, or by changing the focal length of these lenses. The result of these adjustments for PCL^{1C} are shown in Fig. 2a, where the height of the beam on PD can be changed without adjusting the beam width, while the adjustment of PCL^{2C} in Fig. 2b adjusts the width of the beam without affecting the height. The width adjustment is used to ensure the beam is not too tightly focused on the individual PD elements so that saturation of the elements is avoided (see Ref. [25] and Section V.C). The height adjustment is used to change the magnification of the physical probed line in the flow, either increasing or decreasing. For example, if the length of the line at the focus of the system is 10 mm, then with a ten-element PD that is perfectly filled vertically, each element/channel corresponds to 1 mm in the flow. By increasing the length of the line by two, each channel corresponds to 0.5 mm in the flow, and by decreasing the length of the line by two from its initial length, each channel corresponds to 2 mm in the flow. By increasing the line length, the entire physical line will not be probed since it overfills PD, whereas by decreasing the line length, the entire physical line is probed, but not all PD channels are used.

III. Linear Array Photodiode

A. Photodiode Selection

The linear array photodiode used in previous work by the authors ([1, 2]) is a Hamamatsu S8558 Si PIN photodiode array, seen mounted in its electronics enclosure in Fig. 3a. This is a surface-mounted unit with 16 separate channels, where each channel's element measures 0.7×2.0 mm with 0.1 mm separation between elements, and the window material is a silicone resin. The maximum reverse bias voltage that can be applied is 30 V, and its spectral response range is between 320 nm and 1100 nm. While the stated peak sensitivity is 0.61 A/W at 920 nm, the 532 nm laser used for the line FLDI measurements results in a sensitivity of approximately 0.35 A/W. Because this is a surface-mounted unit, they are typically reflow soldered to printed circuit boards (PCB). As a reflow solder oven was not available at the time of fabrication, the units were carefully fixed and manually soldered to a printed circuit board. Using the maximum stated bandwidth of 25 MHz, the rise time of each element can be estimated to be approximately 14 ns.

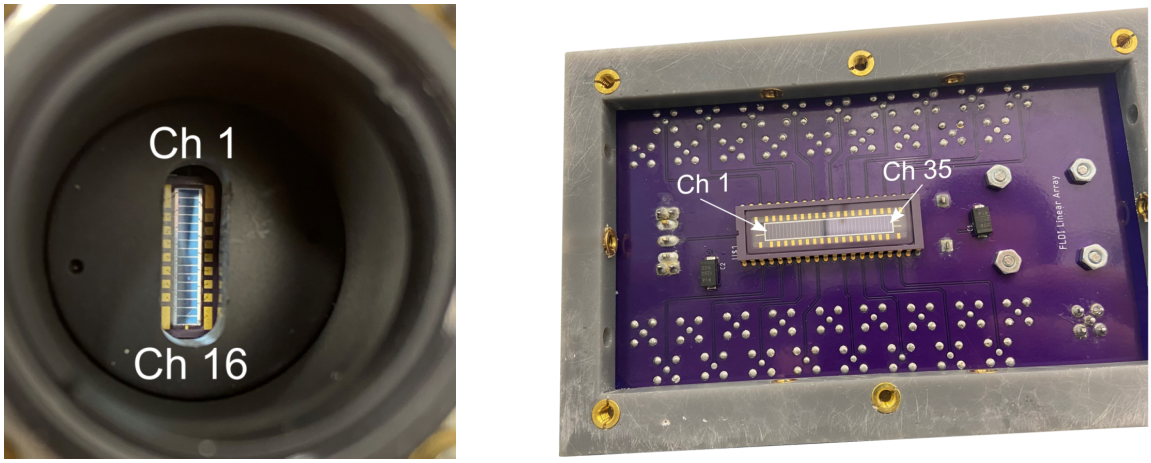

(a) **(b)**

Fig. 3 Images of mounted linear array photodiodes to their respective printed circuit boards/housings for the (a) 16-channel photodiode (S8558) and the (b) 35-channel photodiode (S4114-35Q).

The photodiode selected for the current measurement system is the Hamamatsu S4114-35Q, which increases the channel count from 16 to 35, where each channel's element now measures 0.9×4.4 mm, with a 0.1 mm separation between elements. The wider elements of this photodiode (more than a factor of two) provide a larger buffer for lateral movement of the laser line, either due to beam-steering from the flow itself or higher vibration environments. In contrast to the silicone resin window material of the S8558, this has a window made of quartz, and is mounted in a ceramic 40-pin dual in-line package (DIP), allowing for easier mounting on a PCB than the surface-mounted S8558. The maximum reverse bias voltage of this photodiode is $V_R = 15$ V, half that of the S8558. The S8558 was operated at $V_R = 10$ V with excellent frequency response out past the desired maximum value, and this S4114-35Q can be operated at $V_R = 9$ V with similar results. The spectral response bounds are extended slightly to a range between 190 nm and 1000 nm, with a peak sensitivity of 0.5 A/W at 800 nm. The sensitivity at 532 nm has not yet been tested, but it is stated that at 633 nm, the spectral response has reduced to 0.43 A/W. The rise time using a 1 kΩ load resistor is 50 ns ($V_R = 10$ V at 633 nm). The load resistor for line FLDI measurements is typically 50 Ω to decrease rise times, and so the stated value here is not a lower limit on the rise time (see Section V.D). The dark current of 300 pA is lower than the 1000 pA of the S8558, while its terminal capacitance of 20 pF is higher than the 5 pF values of the S8558. However, the differences between the two linear array photodiodes are minimal enough that testing of the two units in the line FLDI system is the simplest way to compare and contrast their operation.

B. Circuit Board Design

There are two sub-assemblies of the linear array photodiode system. The first is the PCB to which the photodiode itself is mounted, which is installed on the line FLDI catch board at the position of PD in Fig. 1. This PCB is then connected via cables (for each channel) to the second sub-assembly, a signal conditioning unit used to convert the current generated by the photodiode elements to useful voltage signals that can be digitized by the data acquisition system (described in Section IV). The PCB layout of the photodiode mounting sub-assembly is shown in Fig. 4a, where the photodiode is mounted near the center of the 15 cm $\times$ 9.7 cm board. Images of the front and back of the fully assembled/populated PCB are shown in Figs. 4b and 4c, respectively. An on-board mount for a 9 V battery is placed at the center-bottom of the board, and to the left of the battery is an optional input for an external power supply. A toggle switch at the center-top of the board allows the user to select either the battery or external power supply to provide the reverse bias voltage to the photodiode. The top of the photodiode is identified with the semi-circular notch, and so the channels increment from channel 1 to 35 from top to bottom in Fig. 4a. In this figure, the top left pad of the photodiode mount is pin 1, and the pin number increments to pin 20 at the bottom left. Pin 21 is located at the bottom right pad, and the pin numbers increment to pin 40 at the top right pad. Pins 1 and 21 (labeled KC in the data sheet) are connected to the power source (battery or power supply depending on the toggle switch position), while pins 11, 20, and 40 (labeled

NC in the data sheet) are connected to the ground plane. Note that the pin numbers do not correspond to the channel numbers; pins 2 through 19 (excluding 11) correspond to the even channels from 2 to 24, while pins 22 through 39 correspond to the odd channels from 35 to 1.

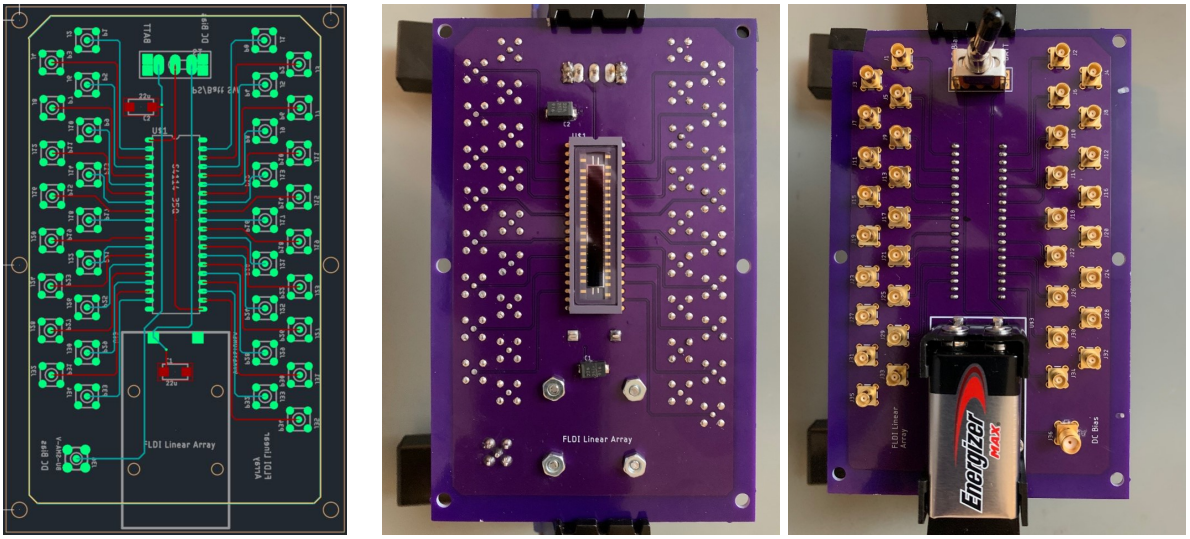

(a) **(b)** **(c)**

Fig. 4 Layout of the 35-channel PCB with linear array photodiode mount, reverse bias 9 V battery or external power supply with toggle switch selection, and breakout connectors. (a) PCB design, (b) front image of assembled PCB, and (c) back image of assembled PCB.

The second sub-assembly is the amplifier unit, whose purpose it is to take input signals from each channel of the first sub-assembly and to output individual channel voltages within the peak-to-peak operating voltage range of the oscilloscope modules of the data acquisition system. For the 35 total channels of the photodiode array, it was decided to construct seven five-channel amplifier PCBs. Each of these boards is a four-layer board, where the first layer is used for integrated circuit (IC) mounting and signal routing, the second layer for the ground plane, the third layer for the split power layer between positive and negative rails (interleaved finger design), and the fourth layer for another ground plane and additional signal routing.

To select the necessary electronics (ICs, passive components, etc.) for the amplifier circuit, the expected incident power for each photodiode channel needed to be determined. For example, the S8558 photodiode has responsivity of approximately 0.35 A/W at 532 nm. The maximum power from the line FLDI laser is 300 mW, and if spread out over the 16 channels evenly (assuming a top-hat profile, not Gaussian), then each channel will have at most 18.8 mW incident power. Multiplying this incident power by the responsivity gives an output current from each channel of 6.6 mW. When a Nomarski prism is used to split the single line into two measurement lines, the maximum incident power on each linear array is then 150 mW, and the per-channel power decreases by a factor of two. Using the 35-channel photodiode, the same 300 mW spread equally over all channels results in a per-channel power of 8.6 mW. From the spectral response plot in the data sheet, the responsivity at 532 nm is approximately 0.38 A/W, giving a per-channel output current of 3.3 mA. For a two-line measurement, this per-channel current decreases to 1.6 mA. In reality, the incident beam shape is not a top-hat profile, but is instead Gaussian, and so the central channels receive a higher incident power while the outer channels receive a lower incident power. These per-channel power values calculated here are upper limits, since there is some loss of power through the optics from the laser to the photodiode. From Section II.F in Ref. [25] on system transmission losses, it was calculated and measured that the transmission of light from the laser to the photodiode was approximately 60%. Using this transmission value (which is not quite accurate due to the inclusion of the extra cylindrical optics here), the per-channel output current is approximately 2 mA for the single-line measurement, and thus approximately 1 mA for the two-line measurement. It is impossible to design a system that is ideal for every measurement condition, and so a best estimate for the expected operating conditions must be chosen in order to move forward. Here, it was thus assumed that the per-channel output current would range from 0 mA to 1.5 mA. To begin selection of the electrical components for the amplifier circuit, the desired output voltage range must be prescribed, and

depends on the data acquisition system (hereafter referred to as the *DAQ*, and discussed in more detail in Section IV). The DAQ has a maximum peak-to-peak voltage of 5.0 V, or −2.5 V to +2.5 V. To ensure the measured signals would never clip at the voltage bounds, the desired output voltage limits were selected to be −2 V to +2 V. With the input (photodiode current limits) and output (DAQ voltage limits) design parameters specified, the electronic circuit design could begin.

Using the data sheet of the photodiode as a guide for the design, two common circuits are outlined. The first is to connect an operational amplifier (op-amp) to each channel, and the second is to operate with a single amplifier for all the channels, although caution must be exercised regarding noise and dynamic range in this mode. The method chosen for the development of the system in this paper is to use a separate transimpedance amplifier (TIA) circuit for each channel. The OPA842 op-amp (Texas Instruments®) was chosen for the TIA, and its implementation for a single channel is shown in the circuit diagram of Fig. 5, and seen in the circuit layout of Fig. 6 (U1). The amplifier operates from a ±6 V power supply, and so there are two separate power planes in the PCB, in addition to a ground plane. The $V+$ and $V-$ power planes are +6 Vdc and −6 Vdc, respectively, and are connected to the board with a three-terminal AMP connector (TE Connectivity). Pins 7 and 4 of the OPA842 8-pin DIP IC are connected to the $V+$ and $V-$ planes, respectively. For both the $V+$ and $V-$ pins, two bypass capacitors are connected in parallel to the ground plane to provide a low-impedance path to ground and reduce noise over a wide range of frequencies. Guidance for choosing these capacitors can be found in the *Board Layout* section of the OPA842 data sheet. The first capacitor is a 0.1 μF ceramic high-frequency decoupling capacitor (C7 and C8 in the circuit diagram), while the second is a 2.2 μF tantalum decoupling capacitor (C1 and C2 in the circuit diagram) which is effective at lower frequencies. Both are necessary for ideal operation of the system due to the wide range of frequencies expected during FLDI data acquisition (from DC up to several MHz). The 0.1 μF capacitor should be placed as close as possible to the IC itself for best results, while the 2.2 μF capacitor can be placed farther away, which is the reason for C7 and C8 being placed closest to the chip, with C1 and C2 in close parallel proximity (Fig. 6).

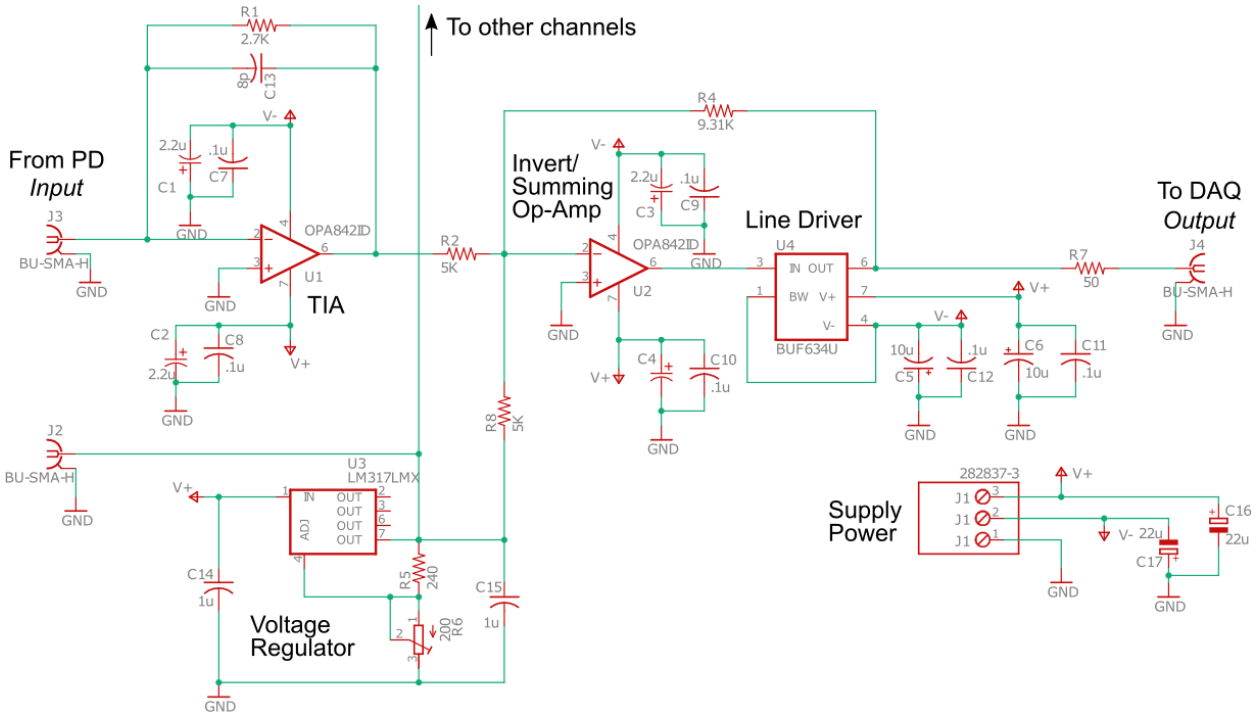

Fig. 5 Circuit diagram of a single channel on one of the seven five-channel amplifier circuit PCBs, including the board ±6 V supply power and the DC offset voltage regulator circuit.

The non-inverting input pin 3 is connected to ground. The photodiode channel output is connected to the inverting input of pin 2, and both a 2.7 kΩ feedback resistor (R1) and a parallel 8 pF capacitor (C13) are connected between output pin 6 and the inverting input pin 2. This feedback configures the TIA to have a response of −2.7 V/mA, with an output range from 0 V to −4 V, and with a bandwidth of approximately 6 MHz. The feedback resistor value was

selected based on the selected typical input current of 1.5 mA from the photodiode. The bypass capacitor, included in parallel with the feedback resistor, is used to ensure sufficient phase compensation to stabilize the circuit. The value of this capacitor was selected to ensure adequate stability while also not affecting the high frequency response that is critical for FLDI measurements, using Eq. (1).

$$C_f \leq \frac{1}{2\pi R_F f_P} \tag{1}$$

where R_F is the feedback resistance and f_P is the desired bandwidth (here, 6 MHz). This equation dictates that the feedback capacitor should be less than or equal to 9.8 pF, and so an 8 pF capacitor was chosen.

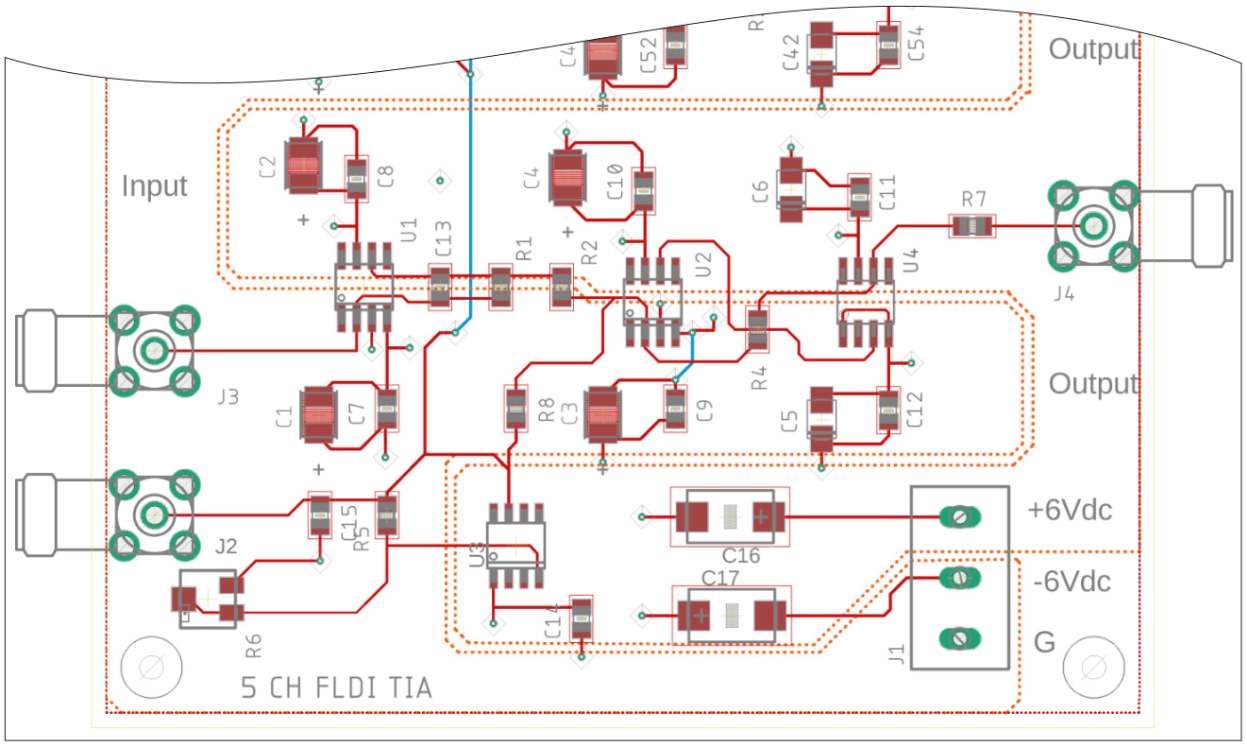

Fig. 6 Circuit board layout of the top-layer components and sub-layer planes, for one of the five channels, including the voltage regulator (bottom left) and supply power connector (bottom right). The interleaved fingers of the $V+$ and $V-$ power planes are visible in dashed orange, top-level traces are red, and bottom-level traces are blue.

The output from the TIA (pin 6) was connected through a 5 kΩ series resistor, and into an inverting summing amplifier in order to invert the voltage signal from the TIA and apply a 2 V shift to center the output voltage about 0 V, maximizing the dynamic range of the DAQ. An OPA842 op-amp was again used here for this purpose, and is shown in the middle of the circuit diagram of Fig. 5 (U2). The non-inverting input of pin 3 was again connected directly to ground, and the $V+$ and $V-$ supply power pins were connected to their appropriate power planes while again being connected to the ground plane through the two parallel bypass capacitors. The output of the OPA842 is not capable of driving a 50 Ω load, so a BUF634 line driver (Texas Instruments®) is used inside the feedback loop of the OPA842 to generate the required output current (output pin 6 of the OPA842 connected to the input pin 3 of the BUF634). It is recommended when driving capacitive loads, such as coaxial cables, that a 50 Ω output resistor be added in series to the BUF634 output to prevent unwanted oscillation. This is the R7 resistor connected between the output pin 6 of the BUF634 and the output SMA connector, J4. The addition of this resistor in conjunction with the 50 Ω load of the DAQ module requires a gain of two to be incorporated into this amplifier stage. The supply voltages of $V+$ and $V-$ for the BUF634 were connected to pins 7 and 4, respectively, and again through parallel bypass capacitors to ground, albeit with larger values for the low-frequency capacitors than for their equivalent in the OPA842 supply lines (now 10 μF, C5 and C6). Pin 1 was connected to pin 4 as recommended by the data sheet for high bandwidth operation, and because

without this connection, a persistent 20 MHz ringing was observed in the output signal. The output pin 6 of the BUF634 is then connected through a 9.31 kΩ feedback resistor (R4) to the inverting input of the inverting/summing OPA842.

In order to shift the voltage output so it is centered about 0 V, an LM317L voltage regulator (Texas Instruments®) is used. This three-terminal, positive-voltage linear regulator can be used for multiple channels, and so each five-channel board has a single, on-board, LM317L IC. It is capable of supplying 100 mA for an output voltage range from 1.25 V to 32 V. The input pin 1 of the 8-pin DIP is connected to the supply voltage $V+$, and to ground through a 1 μF capacitor (C14), which is not required but is recommended. An output capacitor is also not required, but is included in the circuit (1 μF, C15) for improved transient response. The output voltage from the LM317L is given by Eq. (2), where it is stated in the data sheet that I_{adj} is typically 50 μA and can be assumed negligible for most applications.

$$V_{\text{out}} = V_{\text{ref}} \left(1 + \frac{R_2}{R_1}\right) + \left(I_{\text{adj}} R_2\right) \tag{2}$$

In the circuit, R_1 is a fixed-value 240 Ω resistor (R5), and R_2 is a 200 Ω adjustable resistor (R6). The input voltage to the regulator comes from the supply power, and the LM317L generates its own reference voltage of $V_{\text{ref}} = 1.25$ V. To set the value of the adjustable resistor, a current source was used in place of the input from the PD. This current source was set to half the maximum expected output current of the PD (1.5 mA/2 = 0.75 mA), and the variable resistor was adjusted until the output from the circuit was 0 V, the mid-point of the full-scale voltage range. The resistor value for this centered operation of the output voltage was approximately 115 Ω. The output from pin 7 of the LM317L then passes through a 5 kΩ series resistor (R8) before connecting to the inverting input pin 2 of the inverting/summing OPA842.

To demonstrate the input/output relationship of the components in the circuit diagram of Fig. 5, simulations of the circuit were performed in software, with results given in Fig. 7. The simulation output of Fig. 7a shows a plot of the input current from the photodiode on the x-axis, and the corresponding output voltage from the TIA on the y-axis. Because the current input is connected to the inverting input of the TIA, the voltage/current slope is negative. For the expected input current of 0 mA to 1.5 mA from each channel of the photodiode, the output voltage from the TIA ranges from 0 V to −4 V. The inverting and shifting of the OPA842-BUF634-LM317L portion of the circuit is shown in Fig. 7b, where the −4 V to 0 V output from the TIA is now plotted on the x-axis, and the output from the BUF634 is plotted on the y-axis. The output voltage now ranges from −2 V to 2 V, which is the usable range for the DAQ without getting too close to the ± clipping limits of the 5 V peak-to-peak full-scale range. The data of Fig. 7c shows output voltage (input to the DAQ) plotted versus the input current from the photodiode, with a linear regression of all the simulated data points. The y-intercept of −1.87 V is the voltage produced at zero input current (this can be seen later in Section V.D, for example). The slope of the regression, 2.5 V/mA, is the full-system current-to-voltage conversion.

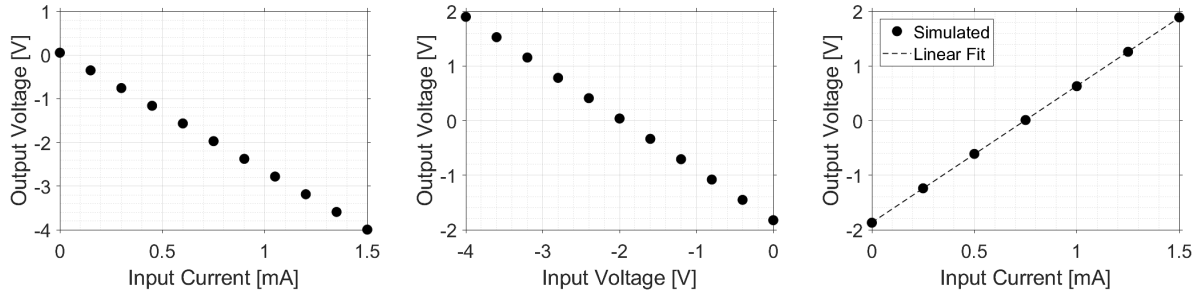

(a) **(b)** **(c)**

Fig. 7 Circuit development stage simulations, for (a) TIA current-voltage conversion, (b) inverting/summing amplifier, and (c) full-system input current to output voltage.

A single amplifier board was constructed and tested to verify correct operation, and that the measured outputs matched the simulations of Fig. 7. Top and bottom views of a single amplifier PCB are shown in Fig. 8a and Fig. 8b, respectively. The five input SMA right-angle connectors are shown at the bottom of the board images, and the five output SMA right-angle connectors are shown at the top. The connector for the supply power can be seen at the top right of the board, and the reference voltage monitor connector for the LM317L is at the bottom right of the board. After successful testing of the single board, six more boards were fabricated, and mounted on top of each other in a

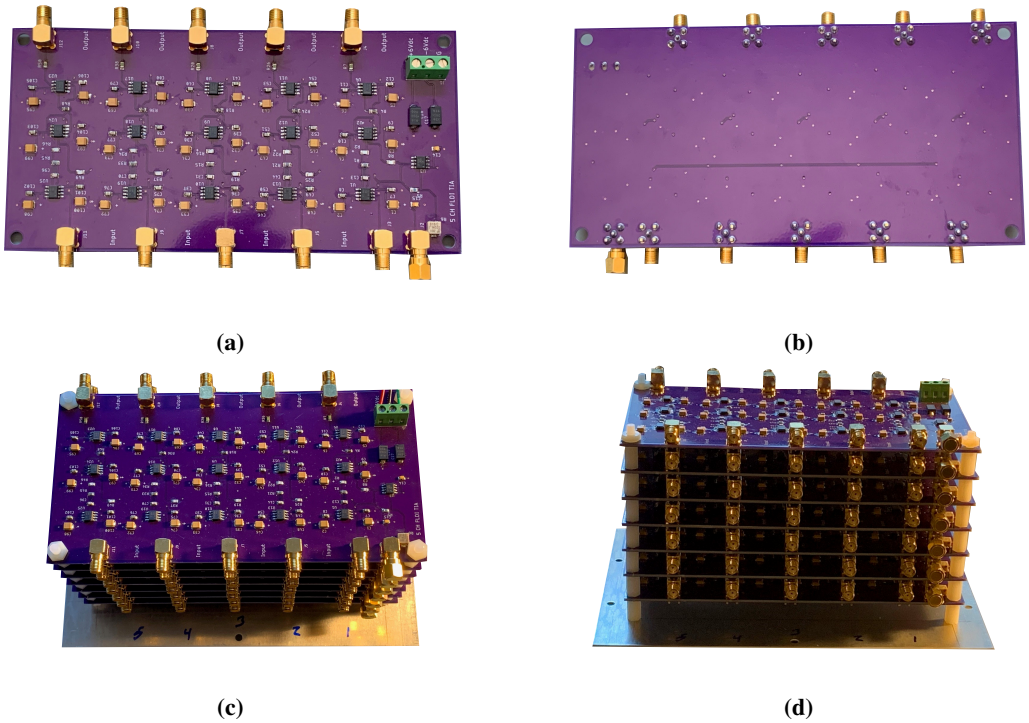

Fig. 8 Images of the (a) top and (b) bottom of a single populated amplifier PCB, and images of the (c) top and (d) side of the full 7-board stacked amplifier system.

compact configuration, using appropriately sized stand-off posts between the boards. Top and side views of this stacked configuration can be seen in Fig. 8c and Fig. 8d, respectively. This stack was then mounted inside a closed housing (shown later in Fig. 12) along with the external power supplies which connect to the supply power connector on each board. This closed housing included a toggle on/off switch and fans for active cooling.

IV. Data Acquisition System

A. Hardware Selection

The development of the data acquisition system was initiated specifically for the needs of the line FLDI system. In the two-point system developed previously (Refs. [25, 31]), only two data channels were required for the two photodiodes, and these were acquired with the MSO 6 series scope (4-channel, 2.5 GHz, 25 GS/s, *MSO6* hereafter). With the development of the 16-point line FLDI system (Refs. [1, 2]), the four channels of the MSO6 scope were no longer sufficient, and a separate higher-channel-count acquisition system was required. The 35-point line FLDI measurements necessitate more acquisition channels, and so the original 16-channel system was expanded further, and functionality added to the user interface based on the ever-changing needs of the end-user.

NI oscilloscope (*scope* hereafter) high-speed modules were used for the development of this system due to their modularity and flexibility for expansion. The linear array FLDI system is only limited in channel count by the photodiode being used, since the laser line itself is a continuous beam created by a combination of cylindrical and spherical optics. The NI PXIe-1092 Chassis was selected for its high slot count (eight), enabling the ability to expand to higher channel numbers than the original 16 planned. There is one PXIe slot and seven hybrid slots, which accept either PXI or PXIe modules. The controller module was a PXIe-8381 with 4 GB/s MXI bandwidth. This controller allows the user to directly control the PIXe systems through a computer. Both fiber optic and copper cable types are supported by this controller, but copper was used because the distance between the chassis and the computer was always less than the maximum length of 10 m. However, having the flexibility to use a fiber optic cable for distance up to 200 m can be helpful for wind tunnel testing, where the chassis may need to be close to the measurement system (e.g., FLDI),

and the computer inside a separate control room (if not using Ethernet extenders). Two eight-channel PXIe-5171R scope modules were initially used to acquire the necessary 16 channels of data, but for this expanded 35-channel linear array photodiode, three more of the same scope modules were added for a total of 40 channels. These scope modules simultaneously sample eight channels at 14 bit resolution, have a maximum bandwidth of 250 MHz, and use SMA connectors for each channel input. The input signals are terminated at 50 Ω, can be either AC or DC coupled, and have five selectable full-scale voltage input ranges (0.2, 0.4, 1, 2, and 5 V).

B. User Interface Development

An image of the starting screen of the user interface for the DAQ is shown in Fig. 9, where the plotting area is blurred for clarity, and zoom-views of select regions of the window are shown in their appropriately colored areas. At the left, the three tabs (discussed later and shown in detail in Fig. 10) are used prior to acquisition to set the desired parameters, including channel voltage details, time/sample parameters, and trigger options. At the bottom left (magenta), general acquisition status is displayed. At the bottom right (blue), the controls for the acquisition are provided. The progression of the data acquisition proceeds as it does with any scope: first, the acquisition parameters are set, then the type of acquisition is selected (calibration/acquisition), and then finally the acquisition is started. This section will describe the procedure and options for the detailed operation of the system, as well as some details and lessons learned throughout the development process. Note, however, that not all functionalities shown in the subsequent images will be detailed.

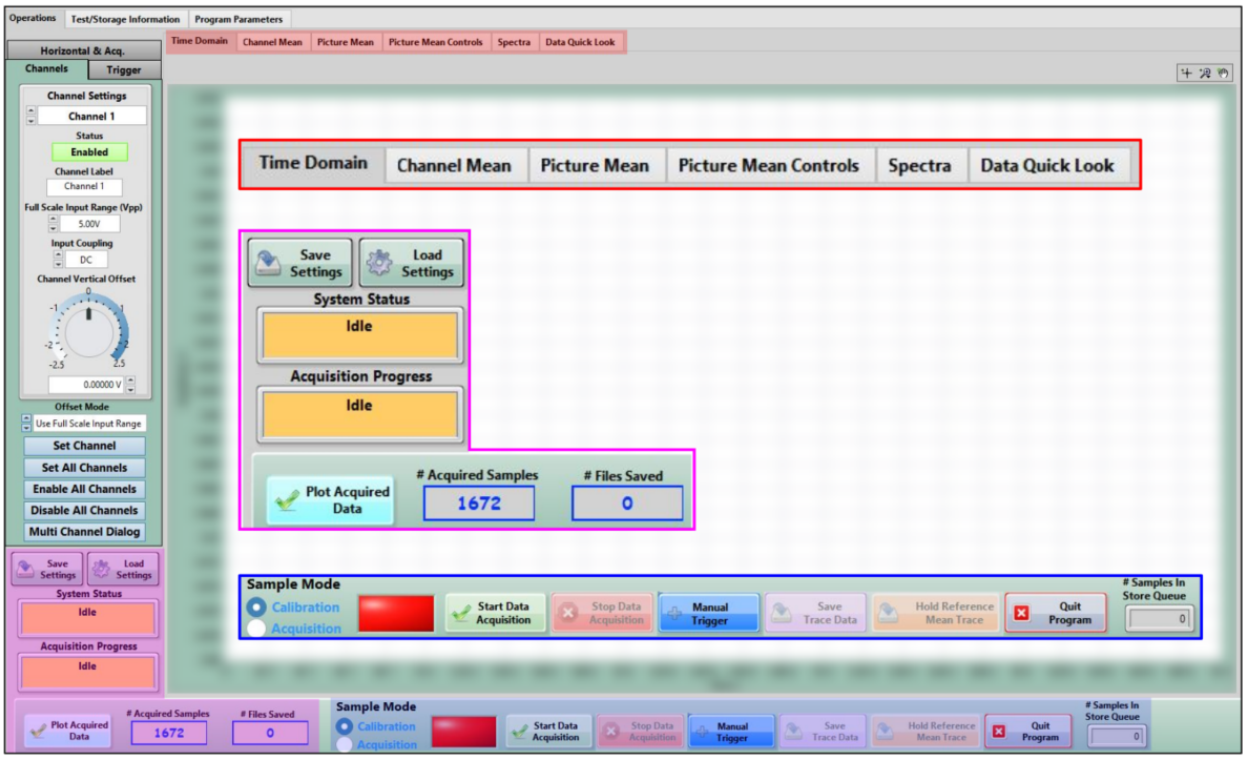

Fig. 9 DAQ LabVIEW user interface starting screen, with plotting area blurred for clarity, and zoom-views of various regions of the window for (red) plotting, (magenta) acquisition status, and (blue) acquisition control.

To begin setting up the system for acquisition, three tabs on the left side of the screen are available and are shown in Fig. 10: *Channels* (Fig. 10a), *Horizontal & Acq.* (Fig. 10b), and *Trigger* (Fig. 10c). The *Channels* tab allows the user to set the vertical (voltage) parameters of the individual channels. At the top of the tab, the channel can either be selected from a drop-down list, or can be scrolled through with the up/down arrow buttons. The channel acquisition can either be enabled or disabled by clicking on the *Status* button, and will change from green to red when disabled. The full-scale vertical range of the measurement is then set (0.2, 0.4, 1.0, 2.0, and 5.0 V), and the input coupling selected (AC or DC). The vertical offset can be changed as well, which does not change the underlying acquired data, but can be

helpful in separating multiple channel signals from each other in the plotting window. Note that each channel can have any combination of these settings. After changing the values in this tab, the *Set Channels* button is pressed to make the changes take effect. If multiple channel settings were changed, the *Set All Channels* button can also be pressed. The selection of each channel and the changing of its settings can be tedious if being done for all 35 channels of the photodiode, so a *Multi Channel Dialog* was created for a more efficient channel parameter setting experience (details of this dialog will be given later in this section). After setting the vertical parameters for each channel, the horizontal parameters are set using the *Horizontal & Acq.* tab shown in Fig. 10b, and are the same for all channels. User defined values are shown in the gray box in the tab, while the rest of the boxes are computed from these values to give more information about the selections. The sampling duration can be set from a list of discrete values from 1 μs to 5 s, and the sample rate from a list of discrete values ranging from 1 Hz to 250 MHz. If a large sampling rate and sampling duration are selected, plotting the full data set for all 35 channels simultaneously can be computationally intensive, and so the *Plotting Subsample Interval* can be changed to an integer value n, which then plots only every n^{th} data point. The *Trigger Wait Time* option is used to set a timeout for the program while waiting for a trigger signal. A countdown clock is displayed on the screen, and once a trigger signal is received, the clock will reset. If no trigger is received within the set duration, the program will exit the acquisition mode, and the user can start the acquisition over again. Finally, in the *Trigger* tab of Fig. 10c, an internal or external trigger can be selected. If internal, extra controls (grayed out in the figure) are available to the user. For the testing performed in this paper, an external trigger signal was used.

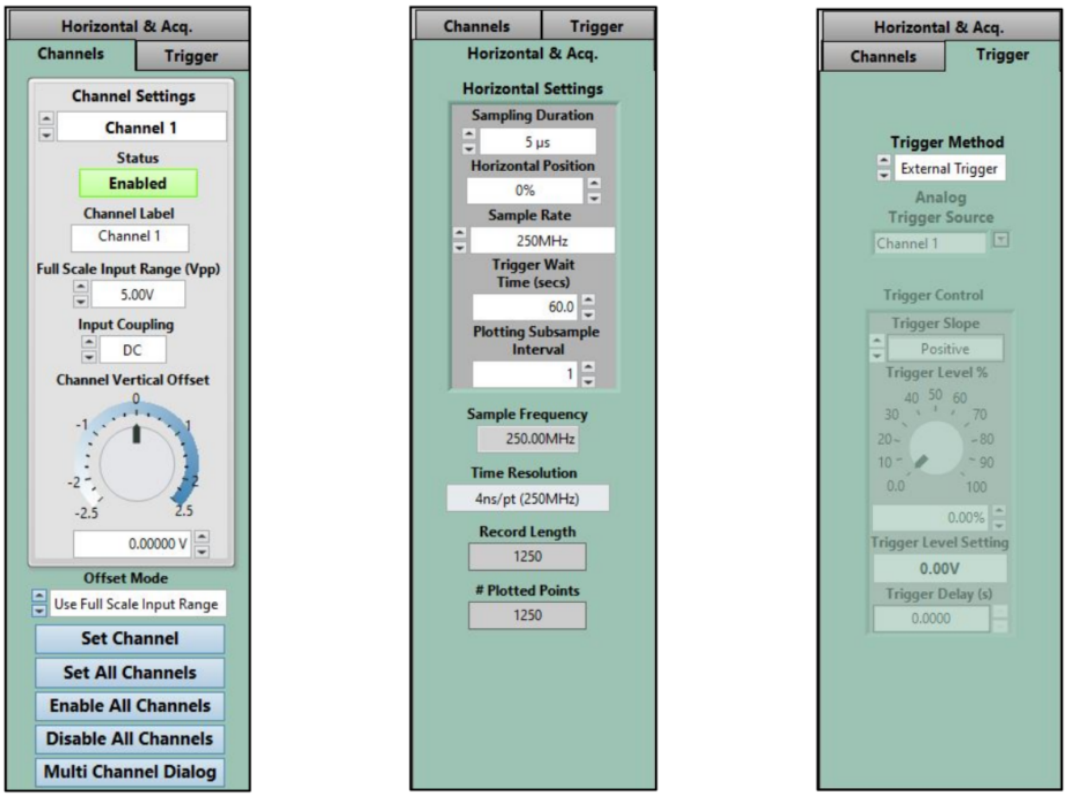

(a) **(b)** **(c)**

Fig. 10 Tabs for defining settings used for acquisition, including (a) each channel's vertical setting and coupling, (b) overall sampling parameters, and (c) input trigger settings.

Setting the vertical parameters for each channel individually in the *Channels* tab of Fig. 10a is time consuming. To reduce time used for this task, the multi-channel dialog was created, which allows for greater flexibility and copy/pasting of repetitive channel assignments. After clicking the *Multi Channel Dialog* button of Fig. 10a, the window shown in Fig. 11 is opened (shown opened to the *Template* tab of the window). Each of the first five tabs corresponds to the channels of a single scope module, each with eight channels. In each of those tab windows, eight of the channel

template windows are given, and can be used to quickly set channel parameters without needing to scroll/select each individual channel prior to changing the settings. This is the quickest way to set channels to different values from each other. If, however, many of the channels require the same settings, the *Template* tab window is used (shown in Fig. 11). Here, a single channel template is given at the left, and check boxes for each of the 40 available channels are given to the right. Buttons below these check boxes allow the user to either select all the channels, or deselect all the channels. The channel template is set to the appropriate values, the channels with which to apply these settings are selected, and the *Duplicate Template Settings* button is pressed. The template can then be changed, other channels selected, and the template duplicated to these channels. After all channels are set to their desired values, the *Apply Settings* button is pressed and the dialog can be exited. If the same settings are to be used in future tests, an initialization file (*.ini*) can be saved using the *Save Settings* button, seen in the magenta highlighted section at the bottom left of the window in Fig. 9. These initialization files can then be loaded at any time using the *Load Settings* button.

Fig. 11 Multi-channel dialog box, showing the bulk settings template tab.

With all the necessary acquisition parameters set, the acquisition can begin. First, the user must select whether to run in *Calibration* mode or in *Acquisition* mode, as shown with the radio buttons in the blue region of Fig. 9. The two modes are functionally the same, but with some slight differences borne out by necessity during the development phase of this instrument. One such difference, for example, is that in calibration mode, the *Plot Acquired Data* selectable push button is always selected, whereas in acquisition mode, it is not. This is due to the overhead required to plot many channels of data at high sample rates when taking data during a line FLDI test. During a typical 30-second wind tunnel run, many data sets are being acquired simultaneously, including multiple freestream and model flow sets. By not plotting data during run acquisition, these data sets can be acquired and saved more quickly, resulting in shorter run times, and allowing for more runs during the day. When the correct sample mode is selected, the *Start Data Acquisition* button is pressed. Status messages at the left of the window aid the user in knowing whether the system is idle, getting ready for acquisition, actively acquiring data, saving data, etc. A dialog window for saving files is brought up, and the user specifies the saving destination folder, file naming convention, and any testing notes. After accepting the settings, a folder is created which contains a text header file (*.hed*) containing all of the settings used for the acquisition. If no data sets are saved before pressing the *Stop Data Acquisition* button, this folder will be deleted in calibration mode, but will not be deleted in acquisition mode. This is because during calibration, acquisition is started and stopped many times as settings are changed and experimental pieces moved into position. This would create many empty folders and was deemed unnecessary. However, during acquisition mode, the folder is not automatically deleted as it is assumed that any acquisition that was initiated will be of use, even if no data is taken and only the header file with test notes is included in

the folder. This can happen during a wind tunnel run where the model failed to inject to the centerline, but where a record of the aborted run is needed. Back in calibration mode after starting the acquisition, data begins to be displayed on the scope software screen for the enabled channels. Data can be saved at any time using the *Save Trace Data* button, which when pressed will save the next acquired/displayed data set. This button can be pressed any number of times, and each time a new file will be saved with all the simultaneously sampled channel data in the saving folder, and the number in the *# Files Saved* box will increment by one. Because none of the acquisition parameters are changed, all saved data sets in this folder have the same header file. If the acquisition is stopped and then started again, a new saving folder is created, with a new header file.

To preserve the fidelity necessary to investigate time varying signals originating from different sources, it is essential that data sampling across all inputs of the data acquisition system be synchronized. This requirement was an important consideration in the design and development of the 40-channel, PXI-based, line FLDI data acquisition system. In order to achieve the desired time coherence in line FLDI measurements, the synchronization of the independent triggering and sampling clocks within each of the five employed high-speed digitizer modules was realized by using the timing and synchronization capabilities of the NI-TClk library supported under LabVIEW. For the line FLDI data acquisition system, functions within the NI-TClk library allow for a single trigger introduced at the Programmable Function Interface (PFI) (AUX I/O) connector to be routed through the PXI backplane to all scope modules, thus enabling them to initiate sampling on the individual channels. A Trigger Clock (TClk) signal controlled by TClk synchronizes the triggers and sample clocks on the individual modules to ensure data sampling coherence throughout the system.

In the red region of Fig. 9, six tabs used for plotting the data in various forms are shown. The default tab is the *Time Domain* tab, which plots the voltage versus time for the acquired signals, whether in calibration or acquisition mode. The x-axis (time) bounds are scaled based on the sampling duration set in Fig. 10b,while the y-axis (voltage) bounds are automatically scaled based on all displayed signals. The ability to establish baseline signal levels and ensure that the extremes of their fluctuations are within the input range of the digitizer is an important consideration when setting up the line FLDI system. These activities help to avoid instances of saturation that would prevent the extraction of useful measurement data. To facilitate the monitoring of the alignment of the optical components and photodiode output signal levels during line FLDI system setup activities, samples are collected for each enabled line FLDI channel and averaged on a per-channel basis. The resultant averaged values are then presented graphically as dots in the *Channel Mean* plot to the researcher to provide real-time feedback regarding system alignment and signal levels. Functionality was developed which allows the researcher to maintain a reference signal trace for each individual channel on demand, enabling active signals to be adjusted as necessary for signal level matching. During development activities it was realized that when aligning the line FLDI optical components in the test section, it was difficult to see signal levels clearly. To overcome this problem, functionality provided within LabVIEW's 2D Picture plot library was used to increase the size of plotted dots allowing the researcher to see them more easily at a distance (in the *Picture Mean* plot). The functionality provided in the 2D Picture library overcame a plot symbol size limitation in LabVIEW's standard graph library. The display of the data in the *Picture Mean* plot can be edited in the *Picture Mean Controls* tab. Functionality includes, but is not limited to, the editing of scatter plot sizes and colors, xy line plot line widths and colors, marker styles, line styles, and axis cosmetics. As mentioned previously, the most important functionality of this plot is to increase the size of the channel markers to be easily viewed from far distances away from the computer monitor when performing the line FLDI system alignment. The *Spectra* plotting tab plots a power spectral density plot of each channel's time series data, and the *Quick Look Data* tab allows the user to load a saved *.bin* file for quick viewing of the signal. This is important during wind tunnel testing between runs, where the user can verify that the signals were acquired correctly, and that voltage levels and fluctuation intensities look qualitatively correct.

While testing the functionality of the line FLDI DAQ system it was observed that the time to save large data sets to the hard drive was excessive. Initially, it was realized in early versions of the LabVIEW application that this was the result of saving collected data samples in ASCII format. The application was then modified to utilize binary file write operations. This resulted in an improvement in data storage times. However, as testing proceeded and larger data sets were collected, a significant increase in data write times was again observed. Investigations into the source code revealed that cause of the problem was the *Transpose Array* function, employed to align channel data into a form that could be more easily manipulated within Excel. Use of this function resulted in repeated allocation/deallocation of system memory to perform the transpose operation. After this function was removed, the time required to write binary formatted data sets to the hard drive was significantly reduced. The cause of the problem was the misuse of the *Transpose Array* function when working with large data sets due to the need for the function to repeatedly allocate/deallocate system memory to perform the transpose operation.

V. System Testing

The image of Fig. 12 shows the full system setup. The linear array photodiode element itself is mounted to the specially designed PCB, with separate cables running out the back of the board for each of the 35 channels, as discussed in Section III.B. A toggle switch on the back of the board (not seen in the picture, but shown in Fig. 4) allows the user to switch between a 9 V on-board battery for low noise measurements, or an external power supply with appropriate connection terminals. The cables from this PCB connect to the back of the black amplifier breakout box via SMA connections. This box contains the necessary power supplies for the amplifier boards in addition to cooling fans and a toggle on/off switch for easy start-up and shut-down. SMA cables connect the front of the amplifier breakout box to the individual channel connectors on the scope modules (eight channels per module), which are housed in the chassis along with the controller module. The controller module is connected to the computer with the large black cables near the top of the chassis, and to the trigger box, which is then connected to a BNC triggering unit for testing.

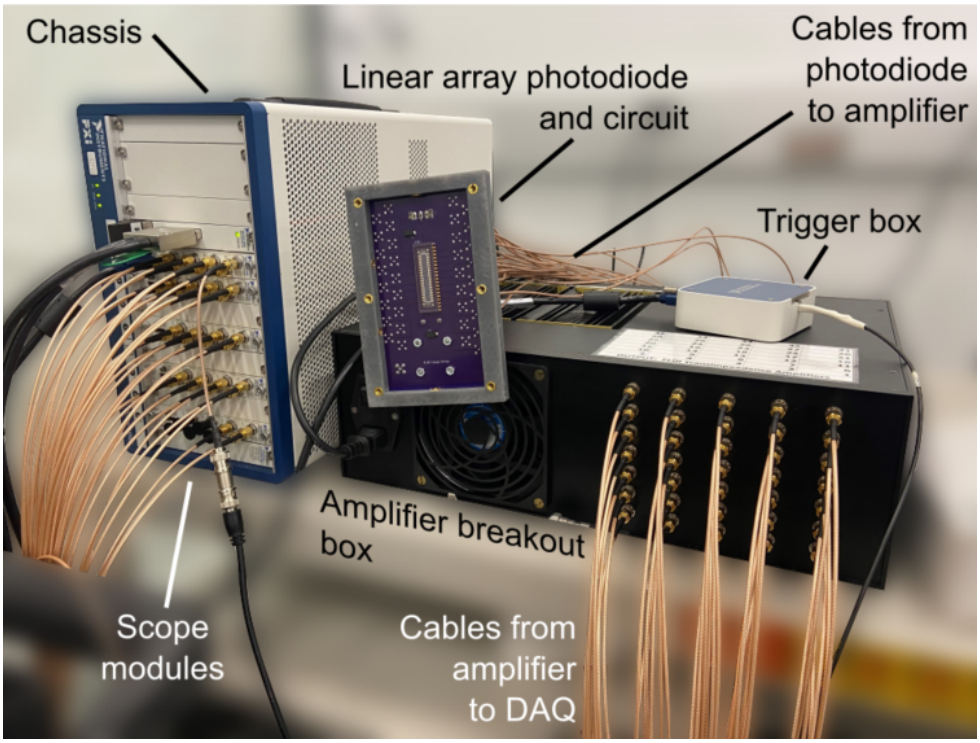

Fig. 12 Image of complete line FLDI acquisition system include photodiode and circuit, amplifier breakout box, scope chassis with modules and trigger box, and connecting cables for all channels.

Incremental testing of the individual systems was performed to ensure all systems were operating as intended/designed. The six testing steps detailed in the following subsections were performed using the equipment listed in Table 1. The specific equipment used for each test, including a schematic of the testing configuration, is given in the subsections below.

A. Test 1: MSO6 and DAQ Comparison

To verify the DAQ was operating nominally, test data were acquired and compared with data acquired with the MSO6 scope, which had been previously used for data acquisition with the two-point FLDI system (Refs. [25, 31]). Triangle, sine, and positive-square waveforms were output from the function generator directly into both scopes, and data were acquired simultaneously. Comparison of these voltage signals between the MSO6 and DAQ are shown in Fig. 13. All waveforms were driven at a frequency of 1 MHz with a 20 dB attenuation of the output signal from the generator in order to keep the output voltage level within the vertical range of both scopes. The horizontal record time for both scopes was set to 2 μs, and has been truncated in the plots to show only one period of the waveform for clarity.

Table 1 Equipment used for full-system testing.

Name	Model	Purpose
Function Generator	Wavetek Model 145 20 MHz Pulse/Function Generator	Generate square/triangle/sine waves for RF modulation input to Bias Tee
Diode Current Controller	ILX Lightwave LDX-3412 Precision Current Source	DC current input to Bias Tee for laser diode driving
Bias Tee	Mini-Circuits ZFBT-6GW	Combine DC and RF current inputs to laser diode
Laser Diode	QPhotonics QFLD-633-10S	633 nm laser diode for regular waveform testing of linear array response
3.6 mm-Square Si Photodiode	Thorlabs DET36A2	Comparison photodiode (small area)
9.8 mm-Diameter Si Photodiode	Thorlabs DET100A2	Comparison photodiode (large area)
Fiber-Coupled Si Photodiode	Thorlabs DET025AFC	Comparison photodiode (fast response)
Comparison Scope	Tektronix MSO6 Oscilloscope	Used to compare data with DAQ

The sampling rate for both scopes was 250 MHz (the maximum available for the DAQ), and the vertical voltage scale (peak-to-peak) for both scopes was $V_{PP} = 2.0$ V.

The acquisition settings remained the same for all recorded signals of Fig. 13, and while a typical two-sided waveform (positive-negative) was used for the triangle and sine function, a one-sided (positive only) square wave was

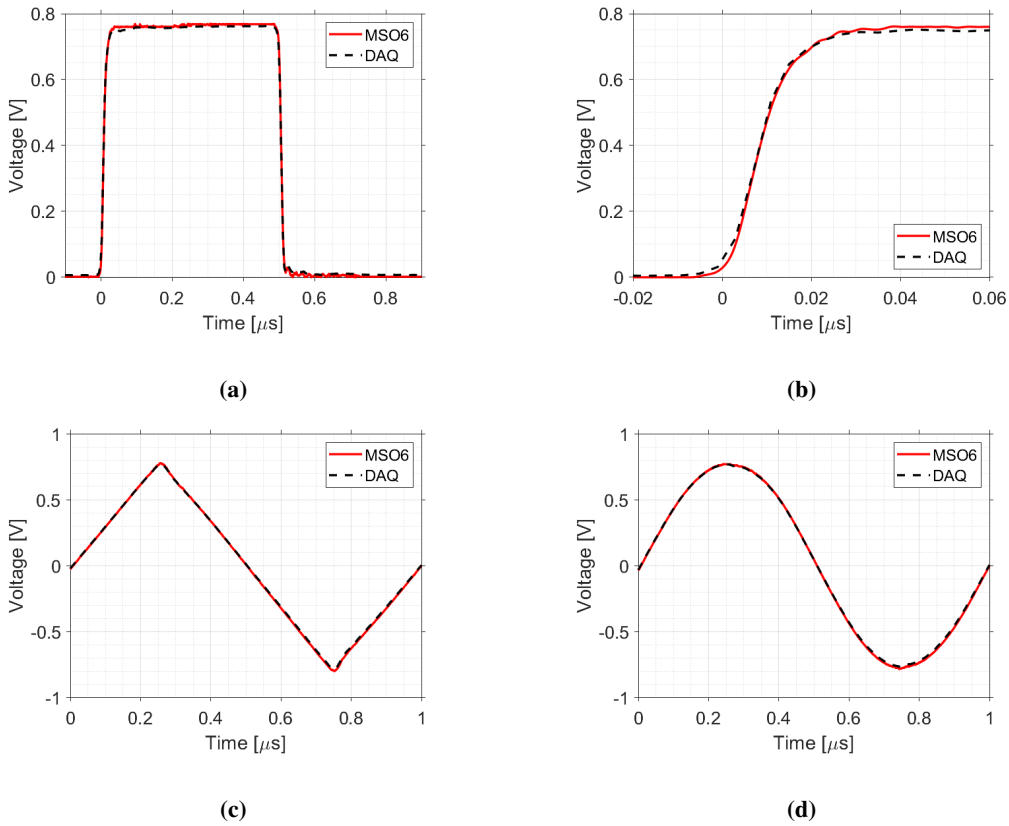

Fig. 13 Comparison of (a,b) positive-square, (c) triangular, and (d) sine waveforms input directly into both DAQ and MSO6 scopes. Plot (b) is a zoom-view of the rising edge of the square wave in (a).

used to get a better rise time measurement starting from the *off* portion of the function as opposed to the negative portion of a two-sided square wave. It was also this one-sided square wave that would be used to drive the laser diode for testing discussed in the following sections. Although the vertical scale of the one-sided square wave appears smaller than the triangle or sine wave, all acquisition used a 2 V peak-to-peak full-scale voltage range (−1 V to 1 V). For all three recorded waveforms, the signal recorded by both scopes is nearly the same, as is expected. In the Fig. 13a zoom plot of Fig. 13b, the rise times for both scopes from the near-step-input of the square function are similar; for the MSO6 and DAQ, the rise times are computed to be 16.8 ns and 16.4 ns, respectively. Note that these rise times were only computed for a single set of acquired data, and no averaging was applied. This limitation on the rise time of the output from the waveform generator will become apparent in following subsections when the waveform is coupled into the laser diode driver. From these results, the DAQ can be used with confidence that measured signals are equivalent to the scope used for previous FLDI testing, and accurately represents input waveforms.

B. Test 2: DET and MSO6/DAQ Rise Time

The testing discussed in Section V.A demonstrated that the MSO6 scope and the DAQ operate nominally the same in terms of their response to various input waveforms. Here, the response of three commercial photodiodes to an input square waveform are compared, again using both the MSO6 scope and the DAQ for comparison (see schematic of Fig. 14a). The input signal to the photodiodes was provided by light emitted from a compact laser diode, mounted in a 14-pin butterfly package with fiber-coupled output. The threshold current for this laser is approximately 55 mA, and so the direct current source was set to a constant value of 60 mA. Without a modulating waveform, the output power from the laser remains constant. A bias tee was used to combine the square wave modulation from the waveform generator, where the current source signal was connected to the DC port and the waveform signal was connected to the RF port. The RF+DC output port was then connected to the laser diode package (Fig. 14b), and the output laser light was modulated in the shape of the square waveform. Three commercial detectors were used, all from Thorlabs®: DET100A2, DET36A2, and DET025AFC. The DET100A2 and DET36A2 are not by default fiber-coupled, and so the fiber output of the laser diode was placed a short distance away from the detector to fill the sensor with light. The DET025AFC is fiber-coupled, and so the fiber was connected directly to this detector. All detectors were operated using an on-board battery (Energizer® A23, 12 V) in order to reduce noise from an external power supply. Each detector was then connected separately to both the MSO6 and DAQ scopes, and the signals were recorded (not simultaneously).

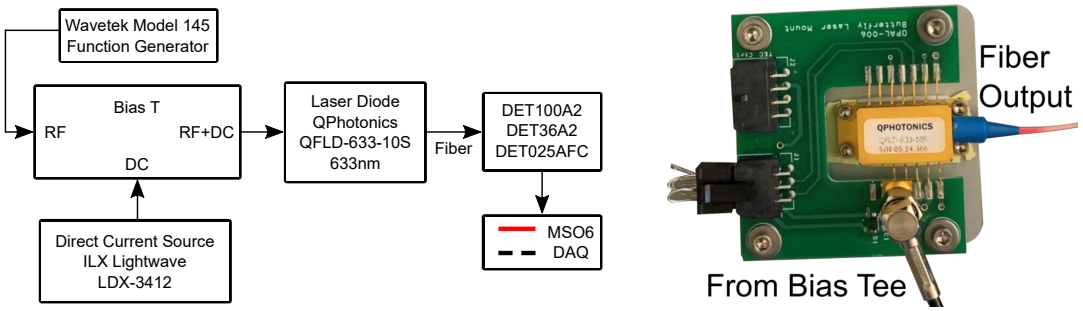

Fig. 14 (a) Schematic of the test setup with three photodiodes and two scopes, and (b) image of the laser diode with bias tee input and fiber-coupled output.

The resulting voltage traces for each detector measured with both scopes are shown in Fig. 15. The responsivity of the DET100A2, DET36A2, and DET025AFC are approximately 0.44 A/W, 0.315 A/W, and 0.36 A/W, respectively. These responsivities roughly match the peak voltage trends seen in the figure, although there is some discrepancy due to the over-fill of the laser diode beam on the sensor element itself. As in Section V.A, the signals from both scopes are nearly identical, and zooming in on the rising edge of the square wave shows that both predict the same rise times. The rise times quoted in the manuals for each detector are 37 ns for the DET100A2, 14 ns for the DET36A2, and 150 ps for the DET025AFC. Measuring the 10% to 90% rise times of a single instance of the square wave, values of 36 ns, 21 ns, and 16 ns were computed for the three respective detectors. While the rise time for the DET100A2 is consistent with

the manual, the other two detectors are not. The measured rise time of the DET025AFC is limited by the waveform generator rise time (see Section V.A). The rise time of the DET36A2 is slightly larger than its quoted value, although it should be able to measure down to the same 16 ns that the DET025AFC did. However, only a single set of data was used for these measurements and calculations, and an average of a series of acquired data sets may be more reliable. Note that all data presented hereafter in the paper were acquired using the DAQ unless explicitly mentioned otherwise.

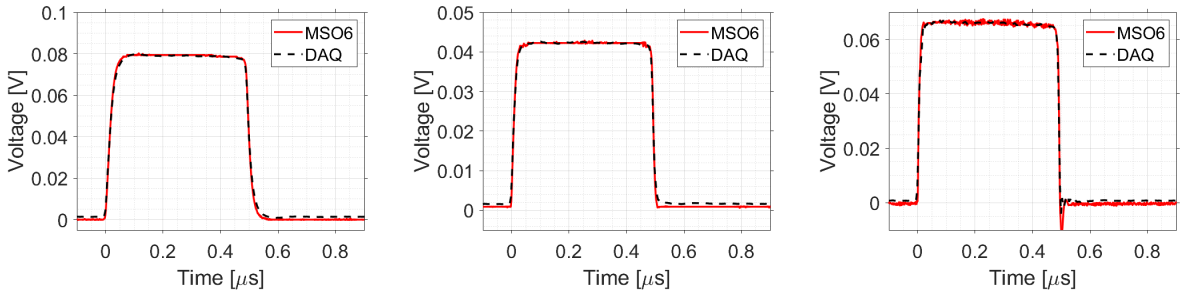

Fig. 15 Comparison of MSO6 and DAQ voltage signals with input laser diode square wave modulation to three detectors, (a) DET100A2, (b) DET36A, and (c) DET025AFC.

C. Test 3: DET Photodiode Saturation

It was demonstrated in Ref. [25] that DC and AC saturation of the photodiode could occur if care was not taken during focusing of the laser beam on the sensor. If too tightly focused, the incident signal amplitude can be distorted and the frequency response degrades (only a plot of the frequency response was shown in that paper). In Fig. 16, raw voltage signals from saturation testing of both the (a) DET100A2 and (b) DET36A2 are shown, with data acquired using the DAQ. Testing was not performed with the DET025AFC because it is fiber-coupled, and did not allow for translation of the fiber tip relative to the sensing element once attached. For each detector, the laser diode fiber output is placed at three distances away from the sensor (far, middle, near), each corresponding to a different fill percentage of the beam on the sensor (far is fully filled, near is tightly focused, middle is in between the other two). As with testing in the previous subsection, the laser diode was driven with a 1 MHz square wave modulation.

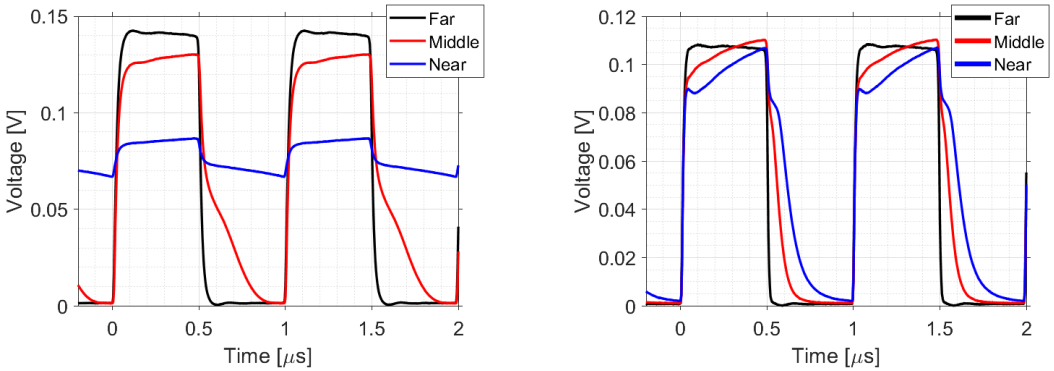

Fig. 16 Detector saturation testing with square wave output from laser diode incident at three positions (far, middle, near) relative to photodiode sensor element for the (a) DET100A2 and the (b) DET36A2.

The resulting voltage traces of this square wave signal incident on the photodiode sensors are shown in Fig. 16, where two periods are shown over the sampling duration of 2 μs. When the laser was not tightly focused on the sensor

(far-black), the square wave is accurately represented, with the same shape as in Fig. 15. As the laser beam was brought into tighter focus on the sensor (middle-red, near-blue), the shape of the square wave input becomes distorted. While the results presented here are not comprehensive, they nonetheless provide further examples of reasons to be cautious regarding the focusing of the laser beam on the photodiodes, this final often overlooked step of the FLDI alignment procedure.

D. Test 4: Linear Array with TIA Circuit

After demonstrating that the DAQ system worked as expected (and performed in a manner equivalent to the MSO6 series scope), the linear array photodiode was connected through the TIA circuit to the DAQ (see schematic of Fig. 17), and the laser diode square wave pattern shined onto the linear array elements. First, the laser was shined onto the central element on the array in order to measure a rise time of this central channel. The rise time quoted on the specification sheet of the S4114-35Q is 50 ns, for a reverse bias voltage of $V_R = 10$ V, a load resistance of 1 kΩ, and a wavelength of 655 nm. With a load resistance of 50 Ω, a reverse bias voltage of $V_R = 9$ V, and an incident wavelength of 633 nm, the rise time was measured to be 31 ns using the square wave rising edge signal. For the S8558 linear array, the rise time is not quoted, but using the cutoff frequency of 25 MHz ($V_R = 10$ V, $R_L = 50$ Ω, $\lambda = 830$ nm, at −3 dB) and the RC low-pass filter model ($\tau = 0.35/f_{3dB}$), the rise time is computed to be 14 ns.

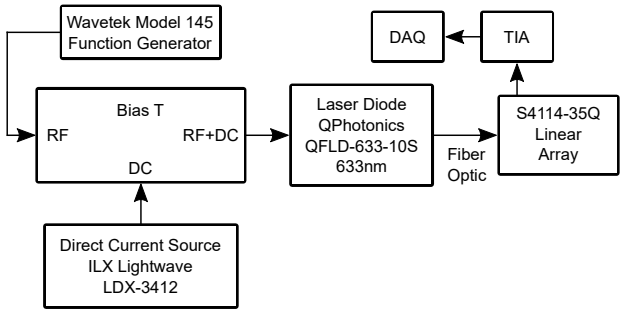

Fig. 17 Schematic of the fully integrated linear array, TIA circuit, and DAQ for laser diode square waveform illumination testing.

To evaluate the simultaneous acquisition of all 35 channels on the linear array photodiode, data were taken of the laser diode Gaussian beam shape being driven with a square waveform at 1 MHz, at five successive distances away

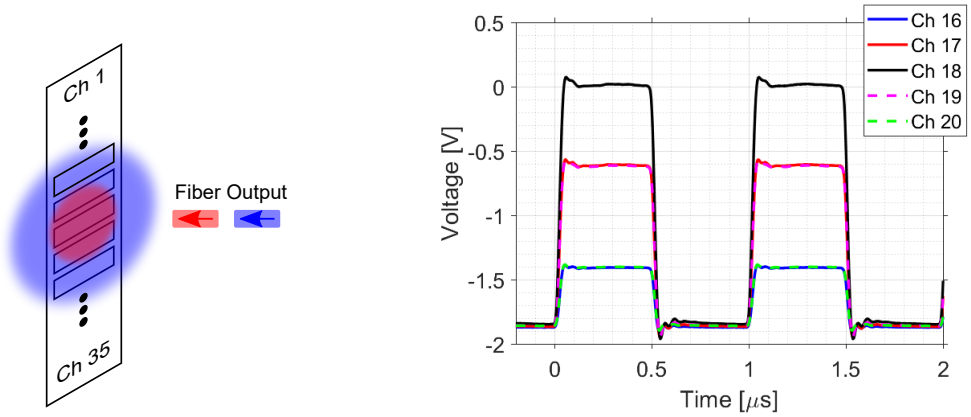

(a) **(b)**

Fig. 18 (a) Schematic of the beam shape testing with two fiber output positions depicted (red, blue), and (b) plot of five channels for closest fiber position ($d = 25.4$ mm) to the linear array.

from the array itself. A schematic of the testing configuration is shown in Fig. 18a, where two of the five total fiber positions are shown with red and blue colors. Since the beam output from the laser diode fiber is divergent, the closer the fiber output is to the array, the fewer the channels should register signal, and with higher intensities (red in schematic). When the fiber is pulled away from the array, more channels will register signal but with overall lower intensities (blue in schematic). The five positions of the fiber from the linear array are 25.4 mm, 31.8 mm, 47.5 mm, 76.2 mm, and 101.6 mm.

At the closest fiber position relative to the linear array (d = 25.4 mm), roughly five of the 35 channels were illuminated, and two periods of the square waveform can be seen in Fig. 18b. The beam is centered on channel 18, the two adjacent channels on each side (17 and 19) have lower but equal peak intensity, and the two outer channels on each side (16 and 20) have the lowest but equal peak intensity. The shape of each channel's voltage signal is the same, albeit scaled vertically based on the amount of power incident on the channel.

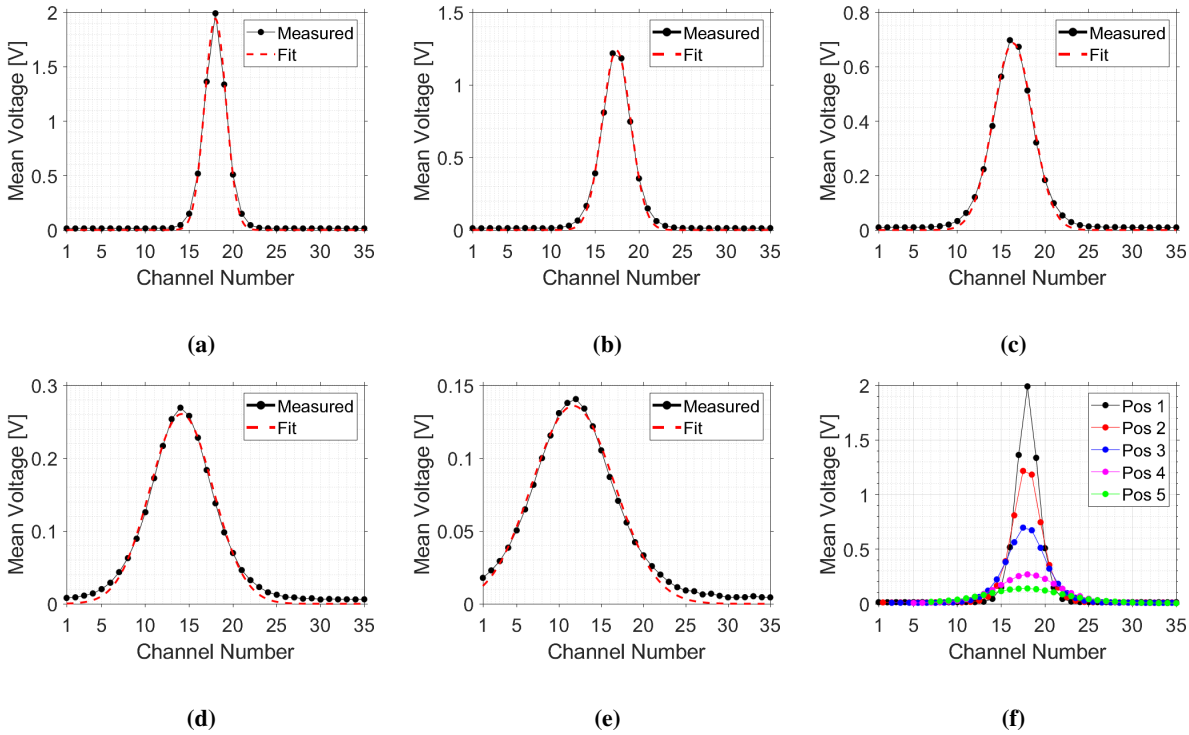

Fig. 19 (a-e) Mean voltage versus channel number for five positions of the laser diode fiber output from the linear array photodiode: (a) 25.4 mm**, (b)** 31.8 mm**, (c)** 47.5 mm**, (d)** 76.2 mm**, and (e)** 101.6 mm **(note different vertical scales). (f) Combined mean voltage plot for all five positions, shifted to align peak intensity position.**

By calculating the mean voltage for each channel (using the top of the square wave profile) and plotting this mean voltage versus channel number, the incident laser diode beam shape can be visualized. This can be seen plotted in Figs. 19(a-e), where (a) is for the closest position of the fiber relative to the linear array, and (e) is for the farthest. As expected, the width of the measured beam shape increases as the fiber is moved farther from the linear array, and the magnitudes of the mean voltage decrease (note that the vertical scale is not the same for Fig. 19(a-e)). The beam also appears to shift from a position centered on the array to a position near the lower channel numbers; this is because the fiber was angled slightly upwards in its mount, and while it was centered for the closest position, the center of the beam moved upwards on the linear array (to lower channel numbers) as the fiber was moved to farther positions. The red dashed lines on each plot are Gaussian fits to measured data points, showing good agreement between the data and the expected Gaussian beam shape emitted from the laser diode fiber output. In Fig. 19f, measured data from all five positions is plotted together, and positions 2 through 5 have all been shifted such that they are centered at the same channel as position 1 (Fig. 19a). Here, both the expanding beam shape and the decreasing mean voltage magnitudes for farther fiber positions are visible.

E. Test 5: Linear Array Channel Crosstalk

Crosstalk measurements were performed to ensure the signal measured by one channel does not affect that measured by an adjacent channel (one of the listed features of this photodiode array is its low crosstalk). This is of particular importance for line FLDI measurements, where the high-frequency fluctuations must be spatially resolved with great accuracy. A 1 MHz square wave was again transmitted from the fiber output of the laser diode and made incident on the five central channels of the linear array (16 through 20). An adjustable slit was then placed between the laser fiber output and the linear array, providing a method of isolating the signal to a single channel at a time, and allowing for height adjustment of the slit to test all five channels isolated from one another (see schematic in Fig. 20a). Note that the fiber output remained fixed in height for all five slit positions, so the measured peak intensity decreases away from the central channel, 18.

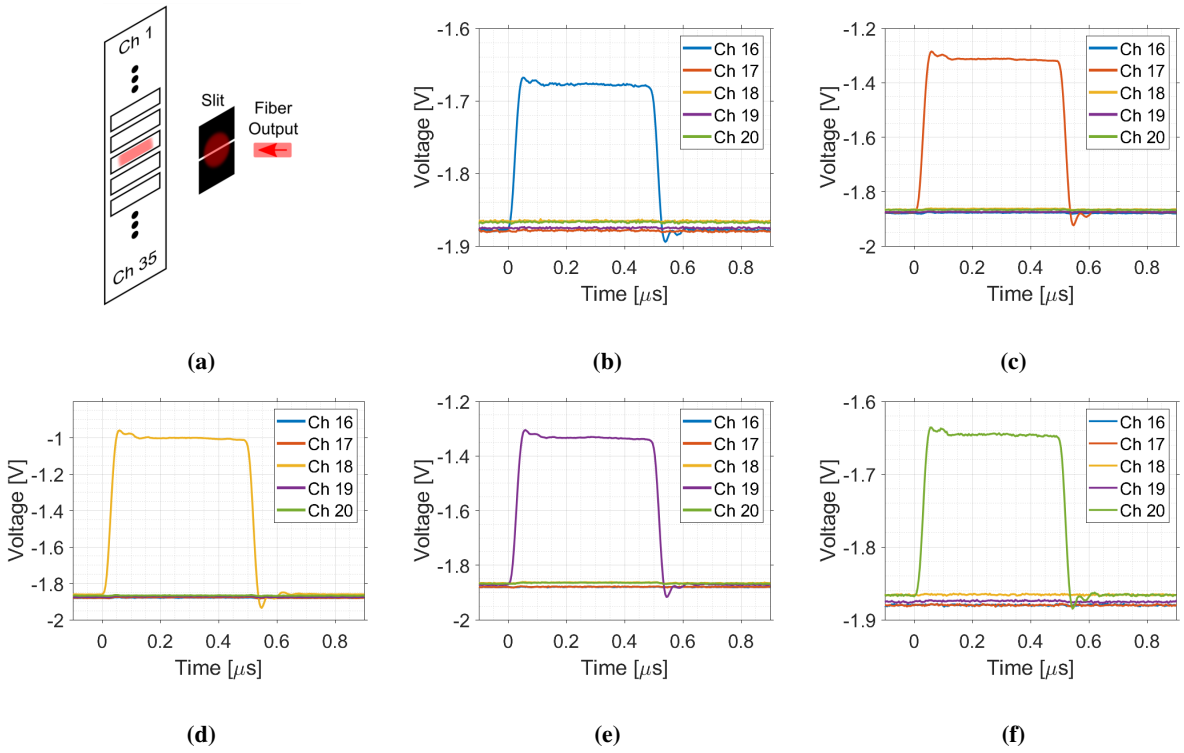

Fig. 20 (a) Schematic of the crosstalk measurements and (b-f) single-period square wave voltage signals of each channel illuminated independently.

Results from the crosstalk testing can be seen in Fig. 20(b-f). The slit was first centered at channel 16, such that light was only incident on channel 16 and not on the other four channels. The slit was then moved down in incremental steps such that each individual channel was illuminated in turn, with the resulting voltage plots shown in Fig. 20b through Fig. 20f for a single period of the square wave laser beam signal. Note that the voltages for each channel in the slit experiments is lower than those of Fig. 18b even with identical laser illumination due to the slit cutting down a large portion of the beam allowed through to the illuminated photodiode elements. Each individual illumination step shows only signal on the illuminated channel, with no signal visible on the adjacent channels, providing sufficient confidence that crosstalk between adjacent channels on the linear array photodiode is negligible.

F. Test 6: FLDI Air Jet Demonstration

After the full integrated systems testing of Sections V.D and V.E, the linear array and DAQ were incorporated into the line FLDI system of Fig. 1 to make measurements of a compressed air jet for demonstration purposes. Although the PCL^{1C} and PCL^{2C} can be used to adjust the size of the line terminating on the linear array, they were both removed for these tests, and so the line seen on the sensor in Fig. 21a (and in the zoom-view of Fig. 21b) has not been altered by a

cylindrical lenses on the catch side of the system. The black dashed outline in Fig. 21b shows the approximate shape of the elliptic line (Gaussian beam profile in both the minor and major axes) incident on the linear array. It can also be seen that the line is not centered vertically on the array, but rather centered between channels 21 and 22. This can also be adjusted with the appropriate optics or by adjusting the linear array itself.

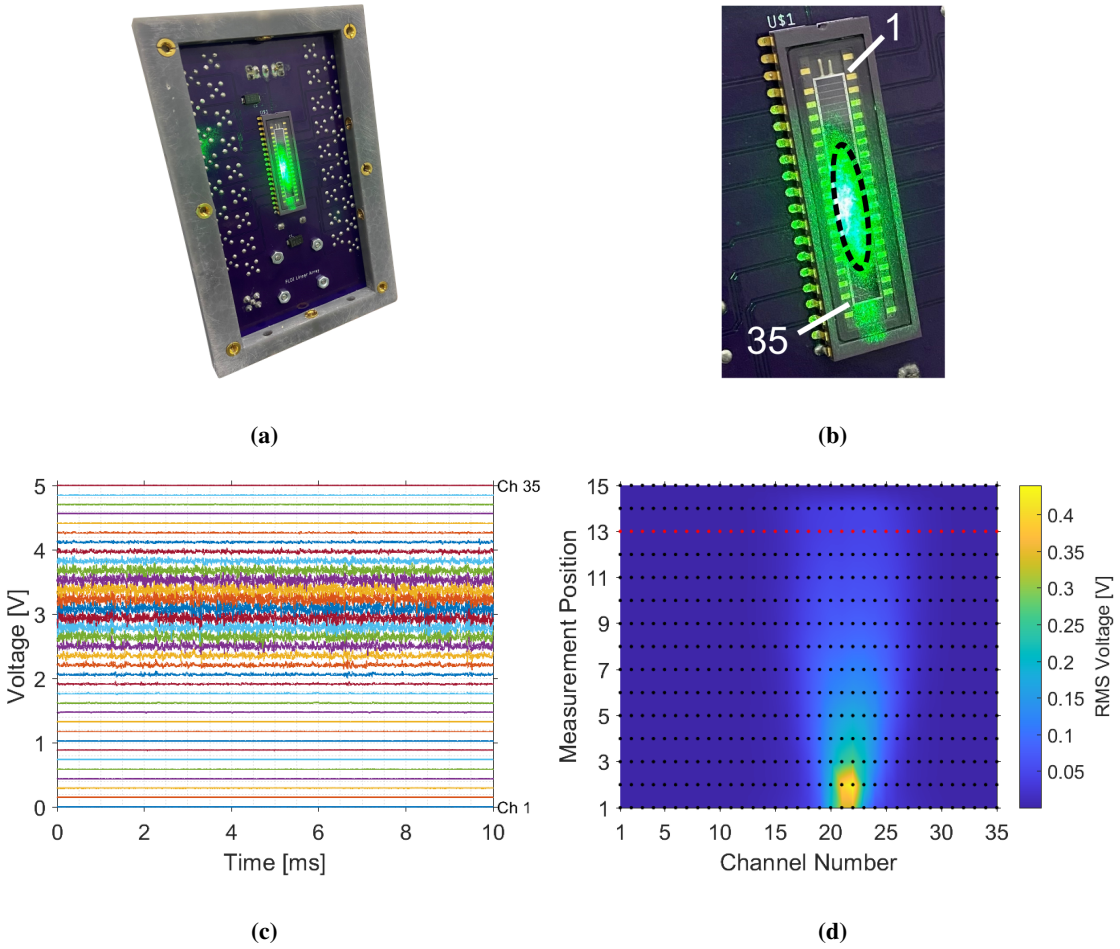

Fig. 21 Images of the (a) mounted linear array photodiode with incident laser line, (b) zoom view of the photodiode element itself with black dashed outline of the laser line, (c) voltage trace of all 35 channels in response to a turbulent air jet, and (d) surface plot of RMS voltage for 15 measurement positions of 35 channels mapping the shape of the jet structure.

Compressed air at approximately 40 psi was issued from a 1.7 mm outer-diameter needle (1.2 mm inner-diameter), which was aligned approximately with the center of the laser line at the line focus (halfway between the pitch and catch boards). Data were then acquired for all 35 channels for a duration of 10 ms at a sampling rate of 10 MHz, with a vertical range of 5.0 V peak-to-peak, DC coupled, with the on-board 9 V battery used to reduce noise. This data acquisition was performed for 15 positions of the needle away from the laser line, starting at its closest position (position 1), and ending at its farthest position (position 15). Note that specific distances of the needle from the laser line were not measured, and so the results presented here are only qualitative. A plot of each channel's mean-subtracted voltage versus time trace can be seen in Fig. 21c, where each channel has been shifted vertically to separate the traces for clarity (channel 1 at the bottom and channel 35 at the top). Here, the larger amplitude noise signals from the turbulent jet are seen near (and surrounding) channel 21, while channels farther away have relatively low amplitude fluctuation signals. The RMS voltage was computed for each channel and for each position of the needle, with results plotted in Fig. 21d. Plotting the RMS voltage this way shows the general structure of the jet, with a high-intensity, small diameter core near the needle exit (position 1), and a lower-intensity, larger diameter jet with increasing distance from the nozzle (higher measurement positions). Each black dot in the figure represents a measured data point (where red dots correspond to the

data shown in Fig. 21c), and only 15 acquisitions of data were required to map the jet structure at 525 discrete points. This 2D jet structure plot can be compared to a similar measurement made using the 16-point line FLDI system (see Fig. 13 of Ref. [2]). The 35-channel measurement provides greater resolution of the jet (although it is at a different magnification), and more measurement data points can be acquired with this increase in channel count.

VI. Conclusions

A specially-tailored data acquisition system was designed, constructed, and tested for use in line FLDI measurements. The system comprises a 35-channel linear array photodiode, an amplifier breakout box, and a National Instruments chassis with five eight-channel high-speed scope modules, for a total of 40 available simultaneous measurement channels. The linear array was chosen for its ability to provide higher spatial resolution than previous line FLDI measurements (35 versus 16), for its similar high-frequency response, and for its wider element sizes that reduce signal drop-out from intense vibrations or beam-steering. The amplifier circuit was designed based on anticipated incident laser power on each channel, and to maximize the dynamic range of the data acquisition system scope modules. The LabVIEW® graphical user interface was updated to more effectively handle the increase of channels from 16 to 35, and to incorporate necessary changes to make the alignment of the FLDI system easier for research that is conducted in an active wind tunnel environment, and to allow for faster file-save times for large data sets during time-sensitive wind tunnel runs.

The systems designed in this paper were systematically tested to ensure proper operation prior to implementation in a line FLDI test. First, the DAQ measurements were compared to a high-quality oscilloscope that has been used for previous two-point FLDI testing. Second, the rise times of various off-the-shelf detectors were compared. Third, the response of these off-the-shelf photodiodes to input laser beams at various distances from the sensor itself was evaluated to determine the saturation effect of beam fill size on the sensor element. Fourth, the linear array photodiode was connected to the amplifier circuit to evaluate the combined performance. Fifth, the crosstalk between adjacent channels on the linear array photodiode was verified to be negligible. Finally, the full linear array acquisition system was implemented in a characteristic compressed air jet test to measure the disturbance fluctuations in a turbulent, and to map a 2D structure of this jet. Results from all the aforementioned testing gives confidence in the system for future high spatial resolution FLDI tests.

While the system was specifically developed for the line FLDI system, the DAQ system has an extra five channels above the 35 required for the line FLDI measurements, and can be used for other simultaneous probe measurements (e.g., Kulite and PCB probes). Implementing this linear array photodiode and acquisition system (which can be easily expanded to more channels with the further addition of scope modules) with a two-line measurement like that detailed in Refs. [1, 2] will allow for highly spatially-resolved measurements of high-frequency flow fluctuations and flow structure velocities.

Acknowledgments

This work was supported by the NASA Hypersonic Technology Project (HTP) and the Transformational Tools and Technologies (TTT) project. We would like to thank Steve Jones and Holt Ripley for their help with moving the necessary equipment for testing from the old lab to the new. The use of vendor and manufacturer names does not imply endorsement by the U.S. Government, nor does it imply that the specified equipment is the best available.

References

[1] Weisberger, J., Bathel, B., Herring, G., Buck, G., Jones, S., and Cavone, A., "Multi-point line focused laser differential interferometer for high-speed flow fluctuation measurements," *Applied Optics*, Vol. 59, No. 34, 2020. doi:10.1364/ao.411006.

[2] Weisberger, J. M., Bathel, B. F., Herring, G. C., Buck, G. M., Jones, S. B., and Cavone, A. A., "Two-Line Focused Laser Differential Interferometry of a Flat Plate Boundary Layer at Mach 6," *AIAA SciTech 2021 Forum*, AIAA-2021-0601, 2021. doi:10.2514/6.2021-0601.

[3] Parziale, N. J., Shepherd, J. E., and Hornung, H. G., "Reflected Shock Tunnel Noise Measurement by Focused Differential Interferometry," *42nd AIAA Fluid Dynamics Conference and Exhibit*, AIAA-2012-3261, 2012. doi:10.2514/6.2012-3261.

[4] Parziale, N. J., Shepherd, J. E., and Hornung, H. G., "Differential Interferometric Measurement of Instability at Two Points in a

Hypervelocity Boundary Layer," *51st AIAA Aerospace Sciences Meeting including the New Horizons Forum and Aerospace Exposition*, AIAA-2013-0521, 2013. doi:10.2514/6.2013-521.

[5] Parziale, N. J., Shepherd, J. E., and Hornung, H. G., "Differential Interferometric Measurement of Instability in a Hypervelocity Boundary Layer," *AIAA Journal*, Vol. 51, No. 3, 2013, pp. 750–753. doi:10.2514/1.j052013.

[6] Parziale, N. J., Shepherd, J. E., and Hornung, H. G., "Free-stream density perturbations in a reflected-shock tunnel," *Experiments in Fluids*, Vol. 55, No. 1665, 2014. doi:10.1007/s00348-014-1665-0.

[7] Parziale, N. J., Shepherd, J. E., and Hornung, H. G., "Observations of hypervelocity boundary-layer instability," *Journal of Fluid Mechanics*, Vol. 781, 2015, pp. 87–112. doi:10.1017/jfm.2015.489.

[8] Ceruzzi, A. P., and Cadou, C. P., "Turbulent Air Jet Investigation using Focused Laser Differential Interferometry," *53rd AIAA/SAE/ASEE Joint Propulsion Conference*, AIAA-2017-4834, 2017. doi:10.2514/6.2017-4834.

[9] Ceruzzi, A. P., and Cadou, C. P., "Simultaneous Velocity and Density Gradient Measurements using Two-Point Focused Laser Differential Interferometry," *AIAA SciTech 2019 Forum*, AIAA-2019-2295, 2019. doi:10.2514/6.2019-2295.

[10] Jewell, J. S., Hameed, A., Parziale, N. J., and Gogineni, S., "Disturbance Speed Measurements in a Circular Jet via Double Focused Laser Differential Interferometry," *AIAA SciTech 2019 Forum*, AIAA-2019-2293, 2019. doi:10.2514/6.2019-2293.

[11] Ceruzzi, A., Callis, B., Weber, D., and Cadou, C. P., "Application of Focused Laser Differential Interferometry (FLDI) in a Supersonic Boundary Layer," *AIAA SciTech 2020 Forum*, AIAA-2020-1973, 2020. doi:10.2514/6.2020-1973.

[12] Hameed, A., Parziale, N. J., Paquin, L. A., Butler, C., and Laurence, S. J., "Spectral Analysis of a Hypersonic Boundary Layer on a Right, Circular Cone," *AIAA SciTech 2020 Forum*, AIAA-2020-0362, 2020. doi:10.2514/6.2020-0362.

[13] Ceruzzi, A. P., Neisess, C., McManamen, B., and Cadou, C. P., "Investigation of Focused Laser Differential Interferometry (FLDI) Sensitivity Function," *AIAA SciTech 2021 Forum*, AIAA-2021-1299, 2021. doi:10.2514/6.2021-1299.

[14] Bathel, B. F., Herring, G. C., Weisberger, J. M., Chou, A., and Jones, S. B., "Simultaneous Focused Laser Differential Interferometry and High-Speed Schlieren in a Mach 6 Flow," *Measurement Science and Technology*, 2021. doi:10.1088/1361-6501/abf67a.

[15] Gillespie, G., Ceruzzi, A., and Laurence, S., "Multi-point Focused Laser Differential Interferometry for Noise Measurements in High-Speed Tunnels," *AIAA Aviation 2021 Forum*, AIAA-2021-2918, 2021. doi:10.2514/6.2021-2918.

[16] Lawson, J. M., Neet, M. C., Grossman, I. J., and Austin, J. M., "Characterization of a Focused Laser Differential Interferometer," *AIAA SciTech 2019 Forum*, AIAA-2019-2296, 2019. doi:10.2514/6.2019-2296.

[17] Lawson, J. M., Neet, M. C., Grossman, I. J., and Austin, J. M., "Static and dynamic characterization of a focused laser differential interferometer," *Experiments in Fluids*, Vol. 61, No. 8, 2020. doi:10.1007/s00348-020-03013-6.

[18] Price, T. J., Gragston, M., Schmisseur, J. D., and Kreth, P. A., "Measurement of supersonic jet screech with focused laser differential interferometry," *Applied Optics*, Vol. 59, No. 28, 2020, p. 8902. doi:10.1364/ao.402011.

[19] Cobourn, J. W., and Schmisseur, J. D., "Focused Laser Differential Interferometry Combined with Schlieren on Hypersonic Hollow Cylinder Flare and Hollow Cylinder Configurations," *AIAA SciTech 2021 Forum*, AIAA-2021-0369, 2021. doi:10.2514/6.2021-0369.

[20] Gragston, M., Price, T. J., Davenport, K., Schmisseur, J. D., and Zhang, Z., "An m by n FLDI Array for Single-Shot Multipoint Disturbance Measurements in High-Speed Flows," *AIAA SciTech 2021 Forum*, AIAA-2021-0599, 2021. doi:10.2514/6.2021-0599.

[21] Gragston, M., Price, T., Davenport, K., Zhang, Z., and Schmisseur, J. D., "Linear array focused-laser differential interferometry for single-shot multi-point flow disturbance measurements," *Optics Letters*, Vol. 46, No. 1, 2021, p. 154. doi:10.1364/ol.412495.

[22] Gragston, M., Siddiqui, F., and Schmisseur, J. D., "Detection of second-mode instabilities on a flared cone in Mach 6 quiet flow with linear array focused laser differential interferometry," *Experiments in Fluids*, Vol. 62, No. 4, 2021. doi:10.1007/s00348-021-03188-6.

[23] Price, T. J., Gragston, M., and Kreth, P. A., "Spatially-Resolved Optical Detection of Jet Screech in a Mach 1.5 Underexpanded Jet with Focused-Laser Differential Interferometry," *AIAA SciTech 2021 Forum*, AIAA-2021-0600, 2021. doi:10.2514/6.2021-0600.

[24] Siddiqui, F., Gragston, M., Saric, W. S., and Bowersox, R. D. W., "Mack-mode instabilities on a cooled flared cone with discrete roughness elements at Mach 6," *Experiments in Fluids*, Vol. 62, No. 10, 2021. doi:10.1007/s00348-021-03304-6.

[25] Weisberger, J. M., Bathel, B. F., Herring, G. C., King, R. A., Chou, A., and Jones, S. B., "Two-Point Focused Laser Differential Interferometry Second-Mode Measurements at Mach 6," *AIAA Aviation 2019 Forum*, AIAA-2019-2903, 2019. doi:10.2514/6.2019-2903.

[26] Birch, B., Buttsworth, D., and Zander, F., "Measurements of freestream density fluctuations in a hypersonic wind tunnel," *Experiments in Fluids*, Vol. 61, No. 7, 2020. doi:10.1007/s00348-020-02992-w.

[27] Benitez, E. K., Jewell, J. S., and Schneider, S. P., "Focused Laser Differential Interferometry for Hypersonic Flow Instability Measurements with Contoured Tunnel Windows," *AIAA SciTech 2020 Forum*, AIAA-2020-1282, 2020. doi:10.2514/6.2020-1282.

[28] Benitez, E. K., Jewell, J. S., and Schneider, S. P., "Focused Laser Differential Interferometry with Contoured Tunnel Windows," *AIAA Journal*, Vol. 59, No. 2, 2021, pp. 419–429. doi:10.2514/1.j060081.

[29] Settles, G. S., and Fulghum, M. R., "The Focusing Laser Differential Interferometer, an Instrument for Localized Turbulence Measurements in Refractive Flows," *Journal of Fluids Engineering*, Vol. 138, No. 10, 2016, pp. 101402–1–101402–10. doi:10.1115/1.4033960.

[30] Houpt, A., and Leonov, S., "Focused and Cylindrical-Focused Laser Differential Interferometer Characterization of SBR-50 at Mach 2," *AIAA Aviation 2019 Forum*, AIAA-2019-3383, 2019. doi:10.2514/6.2019-3383.

[31] Bathel, B. F., Weisberger, J. M., Herring, G. C., King, R. A., Jones, S. B., Kennedy, R. E., and Laurence, S. J., "Two-point, parallel-beam focused laser differential interferometry with a Nomarski prism," *Applied Optics*, Vol. 59, No. 2, 2020, pp. 244–252. doi:10.1364/ao.59.000244.